A Prospective Method for Selecting the Optimal SPECT Pinhole Trajectory

by

Xiangzhi Tao

Medical Physics Program
Duke Kunshan and Duke University

Date:_____

Approved:

_____
James E. Bowsher, Supervisor

_____
Fangfang Yin

_____
Ying Chiang Huang

Thesis submitted in partial fulfillment of
the requirements for the degree of
Master of Science in the Department of
Medical Physics in in the Graduate School of
Duke University

2021

ABSTRACT

A Prospective Method for Selecting the Optimal SPECT Pinhole Trajectory

by

Xiangzhi Tao

Medical Physics Program
Duke Kunshan and Duke University

Date:_____

Approved:

_____
James E. Bowsher, Supervisor

_____
Fangfang Yin

_____
Ying Chiang Huang

An abstract of a thesis submitted in partial fulfillment of the requirements for the degree of Master of Science in the Department of Medical Physics in the Graduate School of Duke University

2021

Abstract

Pinhole imaging is a widely used method for high spatial resolution single gamma imaging with a small required field of view (FOV). Many factors affect pinhole imaging: (I) the geometric parameters of the pinhole imaging system, such as the pinhole diameter, focal length and opening angle; (II) the position, range, sampling interval, and sampling time of the pinhole trajectory; and (III) the image reconstruction algorithm. These differences result in different trade-offs between resolution, sensitivity, noise level, imaging FOV, and data-sampling integrity levels. In pinhole imaging, many different pinhole trajectories might be considered. The conventional approach to assessing different trajectories is to reconstruct images from the various trajectories and then assess which image is best. Such an approach is however time consuming, since (I) image reconstruction is time-consuming and (II) image analysis often requires ensembles of images, where the ensemble is time consuming to calculate, consumes considerable computer storage, and requires investigator time to organize and analyze.

The object of this project is to develop a method to rapidly select the optimal SPECT pinhole trajectory from among several candidate trajectories. Equivalent Resolution Geometric Efficiency (ERGE) is proposed to represent the spatial resolution and geometric efficiency; a higher ERGE means a better trajectory. To verify this metric, two-dimensional and three-dimensional visualizations of the pinhole trajectory are

implemented in software as a way to assess trajectories visually and qualitatively. Several different trajectories are employed, projection data are computer-simulated, including spatial resolution blurring and pseudo-random Poisson noise, and image reconstruction is performed using the OSEM algorithm. The reconstructed images are analyzed to characterize the performance of the different trajectories to assess whether the best trajectory can be determined by the sensitivity and resolution characteristics of the individual pinhole locations that make up the trajectory. Ultimately, the method proved to be effective.

In this study, a relatively simple low-cost prospective method for selecting the optimal SPECT pinhole trajectory has been shown to be effective. Only very fast and simple calculations, utilizing Microsoft Excel for example, are required. The method does not require simulating or acquiring projection data and does not require image reconstruction. The ranking of ERGE matches well with the ranking of reconstructed images based on Root Mean Square Error (RMSE). In clinical and scientific research, many different pinhole trajectories might be considered for pinhole 3D SPECT imaging, but it is too time-consuming to assess each trajectory via reconstructed images. By demonstrating the validity of this method for assessing trajectories, it may facilitate the improved use of 3D pinhole SPECT imaging in clinical and scientific research.

Keywords: Pinhole Trajectory, SPECT, Forward Projection, OSEM, Equivalent Resolution Geometric Efficiency (ERGE), Root Mean Square Error (RMSE).

Contents

Abstract iv

List of Tables viii

List of Figures ix

1. Introduction 1

2. Method 3

2.1 Phantom 3

2.1.1 Head Phantom 3

2.1.2 Hot Sphere Phantom 4

2.2 Imaging System and Trajectory 5

2.2.1 Single-Pinhole System 5

2.2.2 Pinhole Trajectory 6

2.3 Computer simulations 7

2.3.1 Modeling Spatial Resolution and Noise 7

2.3.2 Simulating Projection Data 8

2.3.3 OSEM Reconstruction 9

2.4 Performance calculations 9

2.4.1 Geometric Efficiency 9

2.4.2 Spatial Resolution 10

2.4.3 Equivalent Resolution Geometric Efficiency 11

2.4.4 Root Mean Square Error 12

3. Results 13
3.1 Trajectory 3D Visualization 13
3.1.1 3D Coordinate System 13
3.1.2 Trajectory Verification 14
3.1.2.1 2D Head Phantom Section 15
3.1.2.2 Hot Sphere Phantom 17
3.1.2.3 Convex Hull 18
3.1.3 Trajectory 3D visualization Result 19
3.2 Metrics Comparison 21
3.2.1 Spatial Resolution 21
3.2.2 Geometric Efficiency 22
3.2.3 Equivalent Resolution Geometric Efficiency 23
3.2.4 Root Mean Square Error Comparison 24
4. Discussion 29
5. Conclusions 31
Appendix A 32
Appendix B 38
References 40

List of Tables

Table 1: Trajectories Parameters 14

Table 2: Average Spatial Resolution of Pinhole Trajectories 1-6.....21

Table 3: Average Geometric Efficiency of Pinhole Trajectories 1-6.....22

Table 4: Equivalent Resolution Geometric Efficiency of Pinhole Trajectories 1-6.....24

Table 5: ROI RMSE of Central Slice and Entire Sphere of Pinhole Trajectories 1-6.....27

Table 6: Parameters and ERGE Calculation of Trajectory 1 32

Table 7: Parameters and ERGE Calculation of Trajectory 2 33

Table 8: Parameters and ERGE Calculation of Trajectory 3 34

Table 9: Parameters and ERGE Calculation of Trajectory 4 35

Table 10: Parameters and ERGE Calculation of Trajectory 5 36

Table 11: Parameters and ERGE Calculation of Trajectory 6 37

Table 12: RMSE of ROI Central Slice V.S. Iteration Numbers of Trajectories 1-6 38

Table 13: RMSE of Entire Sphere V.S. Iteration Numbers of Trajectories 1-6.....39

List of Figures

Figure 1: XCAT phantom 3D visualization....3

Figure 2: Parameters for Single-Pinhole System....5

Figure 3: Pinhole Geometry [13]....9

Figure 4: Right-Handed Cartesian Coordinate System....13

Figure 5: 2D Visualization of Trajectory 1, 2, 3....15

Figure 6: 2D Visualization of Trajectory 4 in 50th and 60th slice....16

Figure 7: 2D Visualization of Trajectory 5 in 50th and 60th slice....16

Figure 8: 2D Visualization of Trajectory 6 in 50th and 60th slice....17

Figure 9: Projection data of Hot Sphere Phantom....17

Figure 10: Convex Hull of Trajectories 1-6....18

Figure 11: 3D Visualization of Pinhole Trajectories 1-6....21

Figure 12: Average Spatial Resolution of Pinhole Trajectories 1-6....22

Figure 13: Average Geometric Efficiency of Pinhole Trajectories 1-6....23

Figure 14: Equivalent Resolution Geometric Efficiency of Pinhole Trajectories 1-6....24

Figure 15: OSEM Images....25

Figure 16: ROI Sphere RMSE of Pinhole Trajectories 1-6....26

Figure 17: 40th Slice ROI RMSE of Pinhole Trajectories 1-6....26

1. Introduction

Pinhole imaging is a widely used method for high spatial resolution single gamma imaging with a small required field of view (FOV) [1]. Due to the geometry of its converging beams, pinhole imaging can provide high-resolution images of targets close to the focal point. Collimators serve as an important part of the single photon emission computed tomography (SPECT) imaging chain. Pinhole collimators are widely used for SPECT imaging of small organs or regions of interest (ROIs), such as the thyroid [2], parathyroid [3], breast [4], knee [5], or physiological imaging of small animals [6]. In SPECT imaging for the diagnosis of brain diseases such as Alzheimer's disease (AD) [7] staging and Parkinson's disease (PD) [8], pinhole SPECT might offer higher resolution and detection efficiency than conventional parallel-hole collimators for imaging small FOVs, which are suitable for brain imaging.

Many factors affect pinhole imaging: (I) the geometric parameters of the pinhole imaging system, such as pinhole diameter, focal length and opening angle; (II) the position, range, sampling interval, and sampling time of the pinhole trajectory; and (III) the image reconstruction algorithm. These differences result in different trade-offs between resolution, sensitivity, noise level, imaging FOV, and data-sampling integrity levels. In pinhole imaging, many different pinhole trajectories might be considered. The conventional approach to assessing different trajectories is to reconstruct images from

the various trajectories and then assess which image is best. Such an approach is however time consuming, since (I) image reconstruction is time-consuming and (II) image analysis often requires ensembles of images, where the ensemble is time consuming to calculate, consumes considerable computer storage, and requires investigator time to organize and analyze.

The objective of this project is to assess whether the optimal trajectory, from among several candidate trajectories, can be determined by the sensitivity and resolution characteristics of the individual pinhole locations that compose the trajectory.

To facilitate this process, a metric, equivalent resolution geometric efficiency (ERGE)[1], is proposed to represent both spatial resolution and geometric efficiency. Two-dimensional (2D) and three-dimensional (3D) visualization of pinhole trajectories is implemented, enabling an initial intuitive grasp of various pinhole trajectories relative to the ROI and to intervening tissue that limits pinhole proximity. Several different trajectories are constructed and utilized in computer-simulated data acquisition and image reconstruction, with the computer-simulations modeling spatial resolution and noise. Pinhole trajectories were ranked by an ERGE, and these rankings were compared to root-mean-square error (RMSE) based rankings of reconstructed images.

---

[1] ERGE was proposed based on the suggestion of Dr. James Bowsher.

2. Method

2.1 Phantom

2.1.1 Head Phantom

This study focuses on SPECT pinhole imaging in the brain region, which involves smaller radii of rotation (ROR) than torso imaging and correspondingly potential for higher-quality images.

The 4D extended cardiac-torso (XCAT) phantom [9] displays anatomically complicated human anatomy in a realistic and adaptable manner (e.g., genders, heights, weights, cardiac and respiratory motions, etc.). Consequently, multi-modality, multi-contrast imaging, as with CT, MR, and PET, could also be studied using the XCAT phantom.

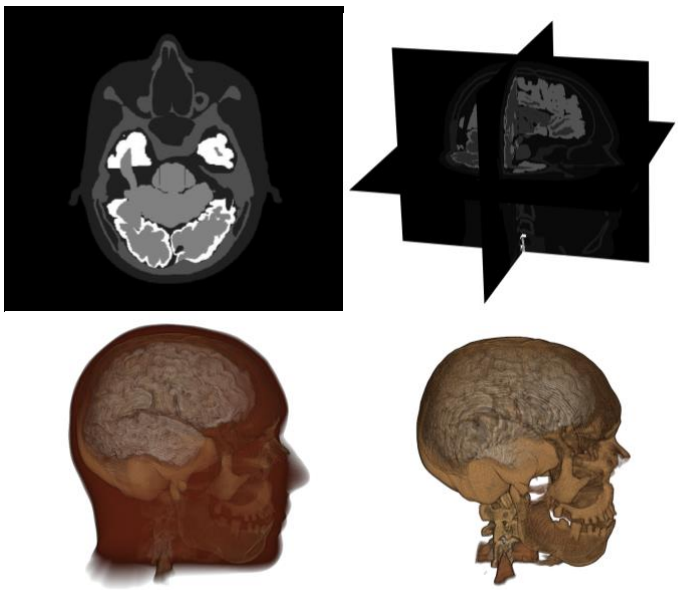

Figure 1: XCAT phantom 3D visualization

In this study, the XCAT phantom software was used to generate a digital anthropomorphic head phantom on a 600 × 600 × 480 fine grid of 0.5-mm-wide cubic voxels, as shown in Figure 1.

2.1.2 Hot Sphere Phantom

A hot-sphere phantom was created, based on the XCAT head-phantom 100 × 100 × 80 course grid with 3-mm-wide voxel size, but with zero activity everywhere except within a 5cm-radius sphere in which the activity is homogenized to one. The center of the sphere is in column 60 row 60 slice 40 of the XCAT head phantom course grid, which in the brain phantom corresponds to the right, posterior section of the brain. The center of the sphere is also the center of rotation (COR) for the pinhole trajectories used in this study. The asymmetric location of the COR, in the right, posterior portion of the brain, results in a large variation in pinhole-to-COR distances, due to the requirement that the pinhole must stay outside the region occupied by the patient's head. Herein the pinhole-to-COR distance is referred to as the radius-of-rotation (ROR).

The hot sphere occupies the same volume as the 5cm-radius region of interest (ROI) over which the brain is imaged in this study. The purpose of this phantom provides a simple method to quickly verify the ROR and detector size is enough to ensure the ROI is fully in the FOV of all angles and that the ROI is completely contained in the convex hull of the pinhole trajectory. It is also necessary to verify that the pinhole

passes through the center plane. The fundamental conditions that must be met for a pinhole trajectory are explained in detail in the subsequent section 2.2.2.

2.2 Imaging System and Trajectory

2.2.1 Single-Pinhole System

A single-pinhole system is considered in this study. It has a circular aperture of diameter d of 3.0 mm, a focal length l of 15.0 cm, and a full pinhole opening angle θ of 90.0°. The focal length is the distance from the camera-image-plane to the pinhole, and the opening angle is the angle formed by the two extreme rays detectable at opposite edges of the camera field of view (FOV). The detector is 30.0 cm wide with a 100 × 100 matrix of 3.0-mm-wide square pixels.

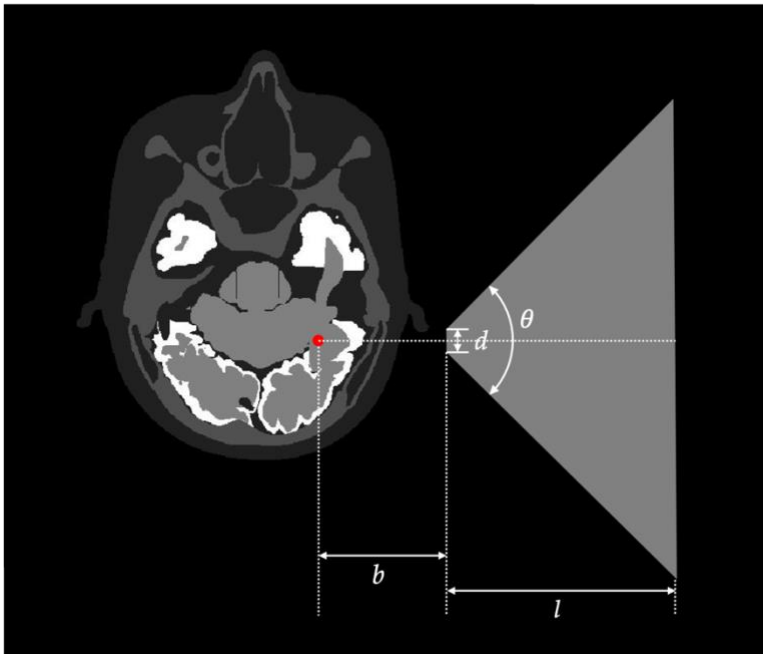

Figure 2: Parameters for Single-Pinhole System

The radionuclide modeled in this study is Technetium-99m, which has a decay channel that emits a 140-keV gamma and has a branching ratio of 0.89. The full width at half maxima (FWHM) of the crystal spatial resolution is modeled as 3.5 mm, which is appropriate for 140 keV gamma rays.

2.2.2 *Pinhole Trajectory*

In this study, all pinhole trajectories are required to meet the following conditions [10]:

(1) The pinhole is restricted from entering a region given by the human body (e.g., head, neck, shoulders, etc.) and the surface of the human body expanded outward by 1.0 cm.

(2) At each position of the trajectory, the FOV of the pinhole detector must include the entire 3D 5cm-diameter spherical ROI. The minimal ROR for achieving this is Equation 1:

$$ROR = \frac{Radius\ of\ ROI}{\sin(\alpha/2)}$$

For a 5cm-radius spherical (ROI), such as considered here, Equation 1 indicates that the ROR should be greater than or equal to 7.1cm.

(3) The pinhole trajectory must satisfy complete-sampling requirements for the 2D region Ω given by the intersection of the spherical ROI and the plane that contains the pinhole trajectory. (In this study, all pinhole trajectories are confined to a plane, but

several different planes are considered.) It means (a) that at each position of the trajectory the FOV of the detector must include the 2D region Ω (as also provided by condition (2) above) and (b) the 2D region Ω must be encompassed in the convex hull of the 2D pinhole trajectory.

(4) The pinhole is as near to the COR as allowed at each place of the trajectory while attaining the aforementioned conditions. That is, the ROR should be as minimal as feasible while still being larger than the ROR's minimum value corresponding to the spherical ROI and the requirement to avoid collision with the patient.

2.3 Computer simulations

2.3.1 Modeling Spatial Resolution and Noise

For each detector bin and source voxel, there is a probability that gamma rays emitted from that voxel will be detected at that bin. Projection simulation and image reconstruction utilize the set of such probabilities for all combinations of bin and voxel. Herein these probabilities are computed using the software package SPECT-MAP, by tracing rays from each bin and through the voxel grid. These probabilities capture effects such as spatial resolution. Components of gamma camera spatial resolution include collimator resolution, intrinsic resolution, and detector bin width. Bin width was modeled by tracing rays from each of 2 by 2 subdivisions of the bin. Pinhole collimator resolution was modeled by tracing multiple rays from each bin subdivision, with these

rays evenly distributed across the pinhole opening. Detector intrinsic resolution was modeled by convolving with a 3.5cm-FWHM Gaussian kernel. Spatial resolution modeling was the same in the forward-projection simulation of projection data and the ordered subsets expectation maximization (OSEM) image reconstruction.

Projection data were scaled to achieve noise levels characteristic of SPECT imaging, with noise then introduced using a pseudorandom Poisson noise generator, with the scaled projection data providing the expected value of the Poisson distribution at each detector bin.

Attenuation and scatter effects were not taken into account in this study.

2.3.2 Simulating Projection Data

Projection data are simulated by summing voxel intensities along the ray paths for all projections of the phantom. In this study, SPECT forward projection was computer-simulated with SPECT-MAP [11]. Due to the limitations of computer performance, but consistent with SPECT spatial resolution, the XCAT head phantom in fine-grid is migrated to a 100 × 100 × 80 coarse grid of 3.0-mm-wide cubic voxels. Projection data were acquired into 3mm by 3mm-wide detector bins at 90 projection angles equally spaced over 270° (3°/projection). Spatial resolution was modeled as 2.3.1 described.

2.3.3 OSEM Reconstruction

Images were reconstructed by Ordered-Subsets Expectation Maximization (OSEM), which is the most extensively used iterative method for reconstructing clinical PET/SPECT images. The reconstructions utilized 15 subsets and up to 30 iterations. Spatial resolution was modeled as 2.3.1 described.

2.4 Performance calculations

2.4.1 Geometric Efficiency

Sensitivity is the proportion of photons emitted from a point source that reaches the camera's surface. Geometric efficiency refers to the geometric component of sensitivity. Theoretical geometric efficiency g of a pinhole is determined by pinhole diameter d, by the distance b from the source to the plane of the pinhole, and by the angle between the pinhole axis and the line from the source towards the pinhole center [12].

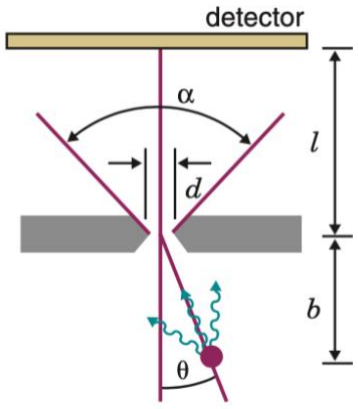

Figure 3: Pinhole Geometry [13]

Equation 2 [14]

$$g = \frac{d^2 \cos^3 \theta}{16b^2}$$

d is the physical diameter of the pinhole, θ is the source-to-detector surface incidence angle, and b is the distance between the point source and the plane of the pinhole. Equation 2 assumes an ideal pinhole such that photons cannot pass through the pinhole material.

In this study, geometric efficiency is calculated for the COR, which is along the central ray of the collimator. Since the central ray passes through the center of the aperture and is perpendicular to the camera crystal, the angle θ is always 0°,

Equation 3

$$g = \frac{d^2}{16b^2}$$

2.4.2 Spatial Resolution

Spatial resolution of a gamma camera image indicates its sharpness and detail. An ideal pinhole collimator has the following point-source spatial resolution R equation using the parameters in Figures 2, 3, and 4.

Equation 4 [15]

$$R = d\frac{l + b}{l}$$

d is the diameter of the circular pinhole aperture, l is the focal length of pinhole, b is the distance between the point source and the plane of the pinhole. If the point source is at the center of rotation (COR), then the b at each pinhole position equals the ROR at that pinhole position. This equation shows that resolution is always best with the source as close as possible to the collimator.

2.4.3 Equivalent Resolution Geometric Efficiency

Equivalent Resolution Geometric Efficiency (ERGE) is used to synthetically describe the spatial resolution and geometric efficiency of the orbit. ERGE is the geometric efficiency calculated at an assumed deterministic resolution. For all trajectories compared, assume that the pinhole has the same spatial resolution at each position.

Since the spatial resolution R is fixed, derived from Equation 4, $d = \frac{R \cdot l}{l+b}$. Substitute into Equation 3,

Equation 5

$$ERGE = \frac{R^2 l^2}{16(l+b)^2 b^2}$$

Note that ERGE can be calculated from the trajectory parameters and pinhole geometry parameters directly. It doesn't require projection data or a reconstructed image.

2.4.4 Root Mean Square Error

Root Mean Square Error (RMSE) is the square root of the Mean Square Error (MSE), and it is used calculate the differences between true value and the value measured. The RMSE aggregates the magnitudes of measurement errors for numerous data points into a single indicator.

Equation 6

$$RMSE = \sqrt{\frac{1}{N}\sum_{n=1}^{N}(M_n - T_n)^2}$$

N is the number of image voxels; T is the true value which is the XCAT head Phantom in this study, and T_n is the value at voxel n of the XCAT head phantom; M is the value of the reconstructed image using a particular trajectory, and the M_n is the value at the n^{th} voxel of the reconstructed image. In general, a lower RMSE is better than a higher RMSE.

3. Results

3.1 Trajectory 3D Visualization

3.1.1 3D Coordinate System

The coordinate convention for pinhole trajectories is defined in the right-handed 3D Cartesian coordinate system *xyz*, show as figure 4.

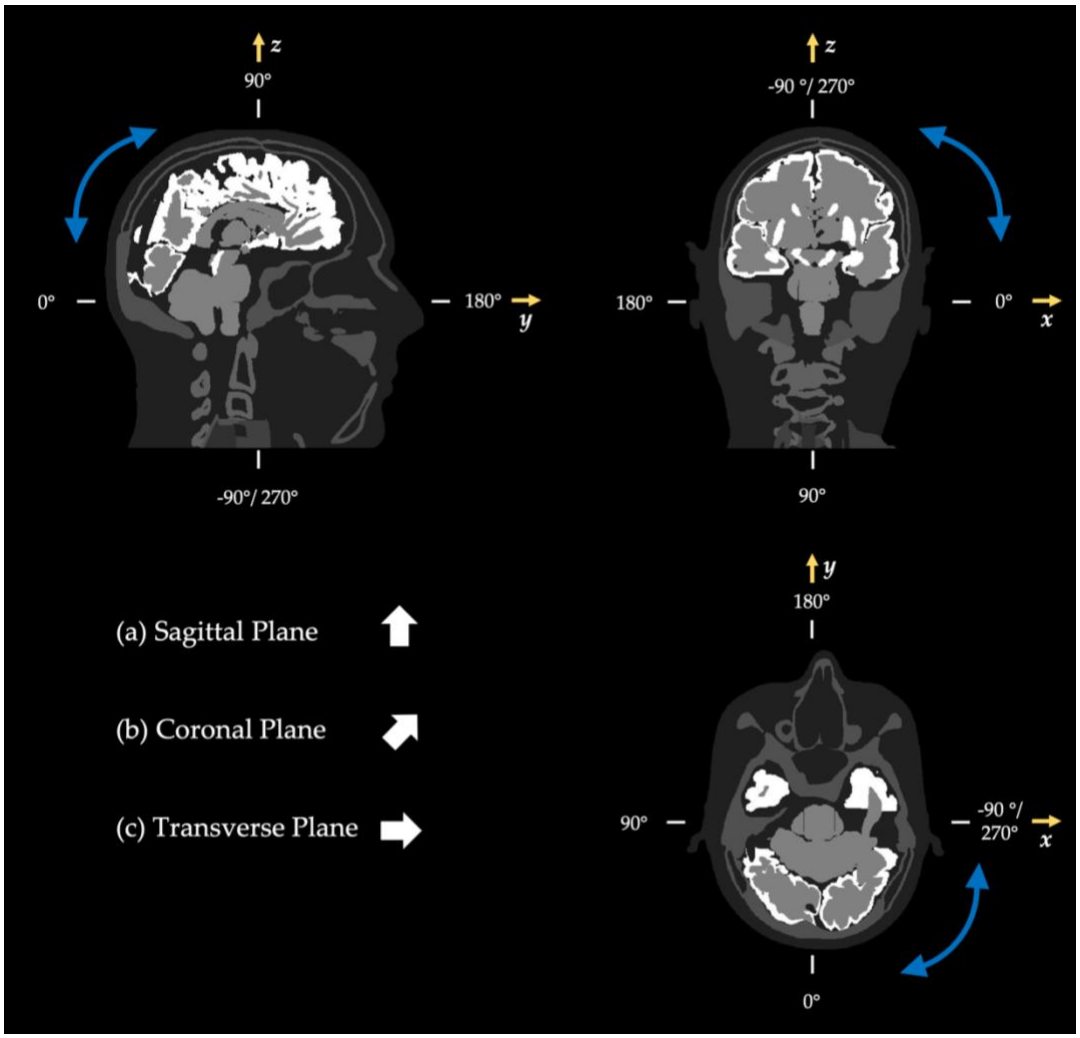

Figure 4: Right-Handed Cartesian Coordinate System

The yellow arrows in Figure 4 indicate the positive direction of the *x*, *y*, *z* axes. The coordinates of the COR and pinhole positions are based on this representation. Sagittal planes are parallel to the *yz* coordinate plane, coronal planes are parallel to the *xz* coordinate plane, and transverse planes are parallel to the *xy* coordinate plane.

3.1.2 Trajectory Verification

All trajectories have the COR at the point (60,60,40) in the Cartesian coordinate system *xyz* and have a total of 90 projections, 3 degrees per projection, covering 270 degrees. The specific parameters of the trajectories are shown in Table 1.

Table 1: Trajectories Parameters

	Plane	Angular Range	ROR		
			Maximum (cm)	Minimum (cm)	Mean (cm)
Trajectory 1	Transverse	-135° → 135°	16.70	7.10	9.45
Trajectory 2	Transverse	-80° → 190°	17.00	7.10	10.79
Trajectory 3	Transverse	-180° → 90°	17.00	7.10	9.36
Trajectory 4	Sagittal	-60° → 210°	17.50	7.10	11.80
Trajectory 5	Coronal	-45° → 225°	14.00	7.20	10.82
Trajectory 6	Coronal	-70° → 200°	13.50	7.20	10.83

3.1.2.1 2D Head Phantom Section

2D head phantom section is used to verify that the trajectories do not enter the region given by the human body. Since the trajectory is in the transverse plane, sagittal plane, or coronal plane, respectively, a 2D head phantom section is selected in each of the three planes, with different 2D coordinate systems *xy*, *yz*, *xz* in the 3D Cartesian coordinate system *xyz*, and with all three planes passing through the COR.

Trajectories 1-3 are established in the coordinate system *xy* of the 40th slice in the transverse plane. Shown in figure 5 from left to right are Trajectories 1, 2, and 3, the circular shading is the ROI in this plane.

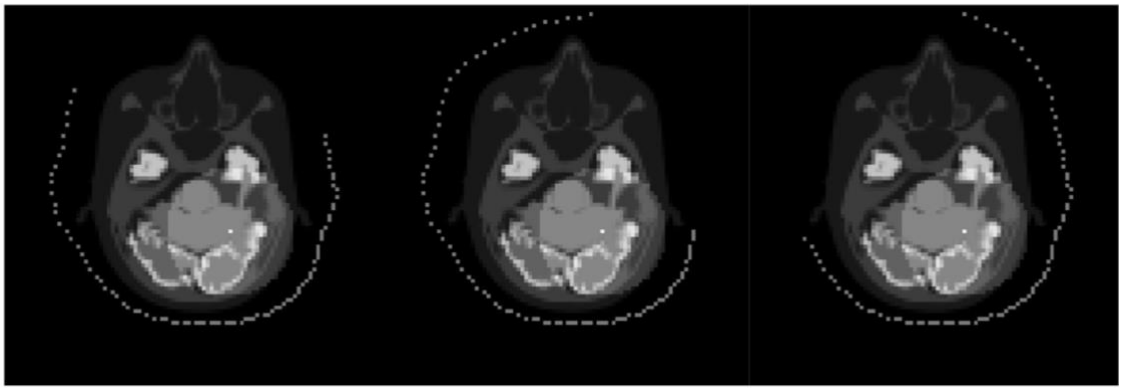

Figure 5: 2D Visualization of Trajectory 1, 2, 3

Trajectory 4 is established in the coordinate system *yz* of the 60th slice in the sagittal plane shown in figure 6 left. This is also the plane where the trajectory runs. However, the sagittal section with the largest area of the head phantom is the 50th slice, so the verification is also performed in the 50th slice show in figure 6 right.

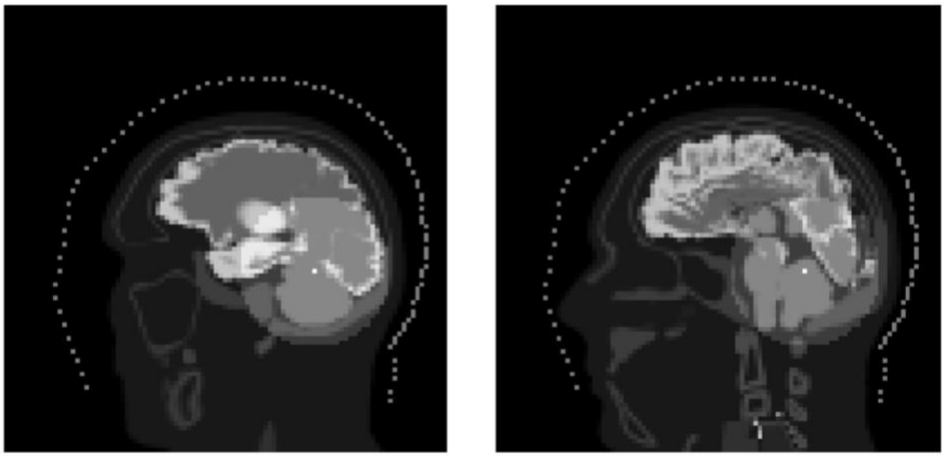

Figure 6: 2D Visualization of Trajectory 4 in 50th and 60th slice

Trajectories 5 and 6 are established in the coordinate system *xz* of the 60th slice in coronal plane, shown in left figure 7 and 8. This is also the plane where the trajectories run. However, the coronal section with the largest area of the head phantom is the 50th slice, so the verification is also performed in the 50th slice show in right figure 7 and 8.

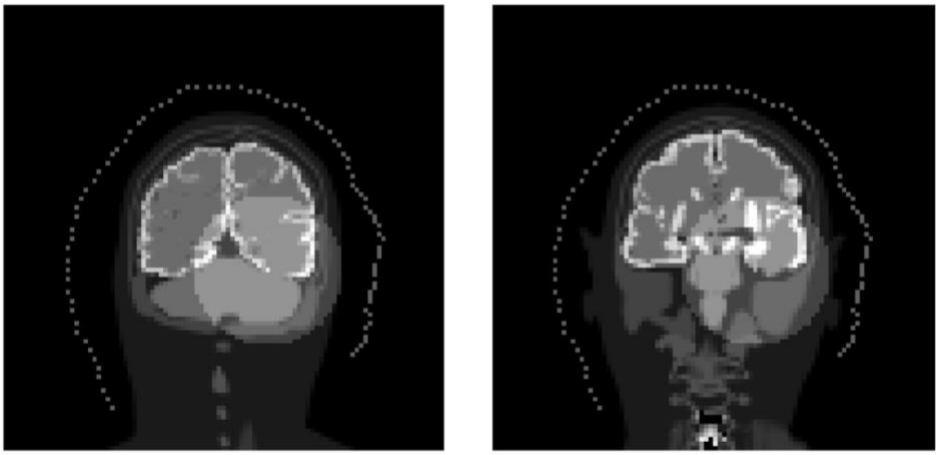

Figure 7: 2D Visualization of Trajectory 5 in 50th and 60th slice

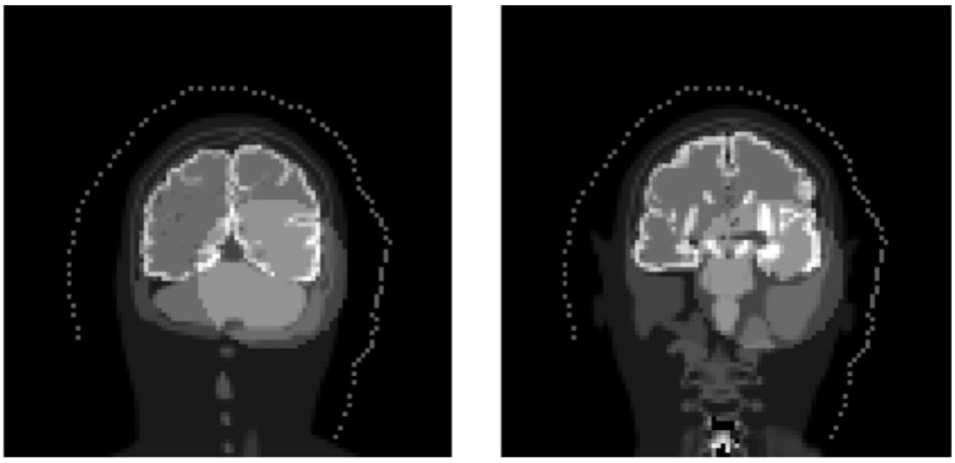

Figure 8: 2D Visualization of Trajectory 6 in 50th and 60th slice

3.1.2.2 Hot Sphere Phantom

For all trajectories 1-6, the hot sphere phantom was forward projected to verify that the ROI is within the pinhole field-of-view (FOV) at all pinhole locations. Figure 9 shows examples of forward projection data for two pinhole locations in trajectory 1.

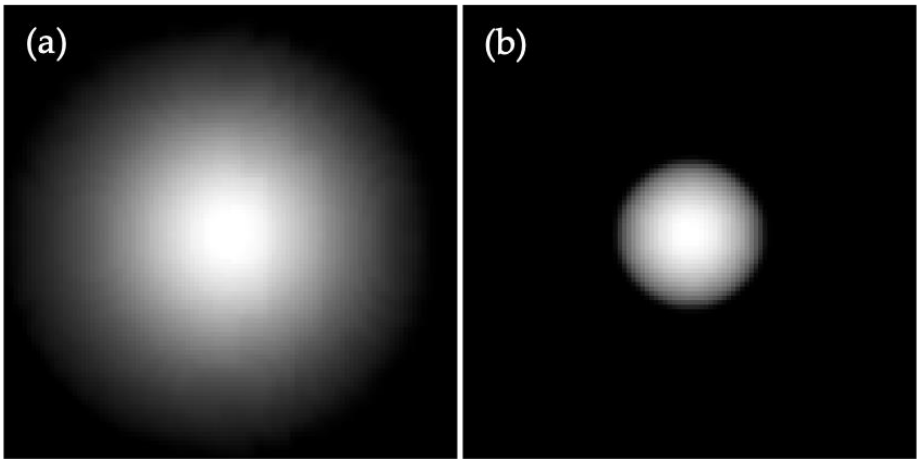

Figure 9: Projection data of Hot Sphere Phantom

Figure 9 (a), (b) show the two angles of projection data at medium contrast, and it can clearly be seen that the hot sphere is completely included in the FOV. Figure 9 (a) shows the projection at the maximum-ROR position, and Figure 9 (b) shows the projection at the minimum-ROR position.The figures show that in both positions the hot ball is fully within the pinhole FOV.

3.1.2.3 Convex Hull

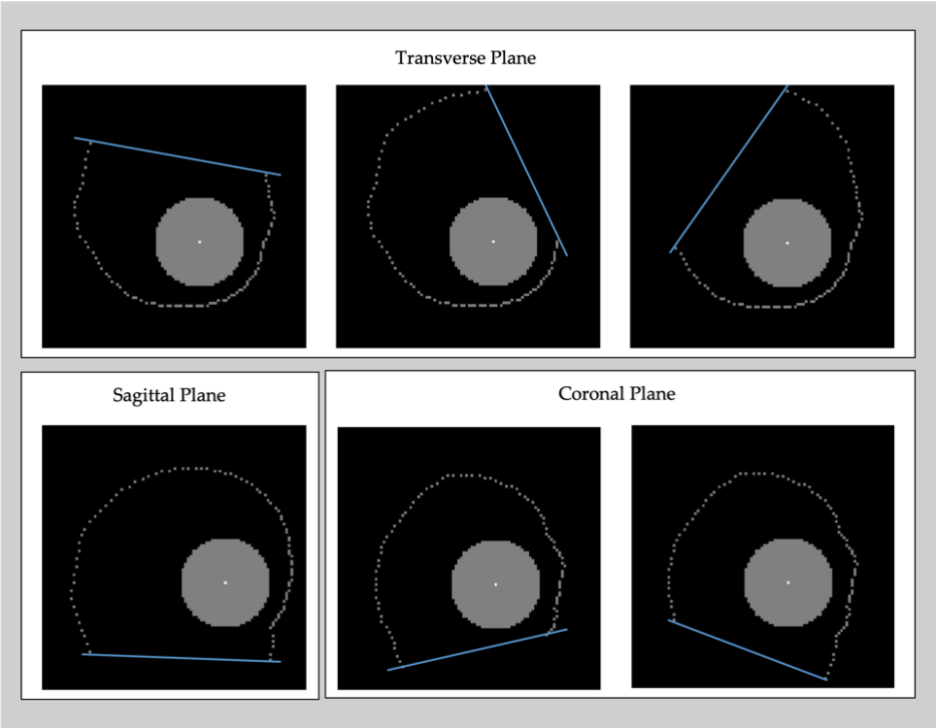

Figure 10: Convex Hull of Trajectories 1-6

In figure 10, the trajectory convex hull, given by the blue auxiliary line and the trajectory points, encloses the ROI. The section used in figure 10 is the center plane of the

hot sphere, which has the largest sectional area ROI in the entire sphere. The convex hulls of all the pinhole trajectories encompass the largest cross-section of the ROI.

3.1.3 Trajectory 3D visualization Result

3D visualization was also employed to verify pinhole position. This 3D visualization included interaction with the mouse, enabling the user to rotate the phantom to any view.

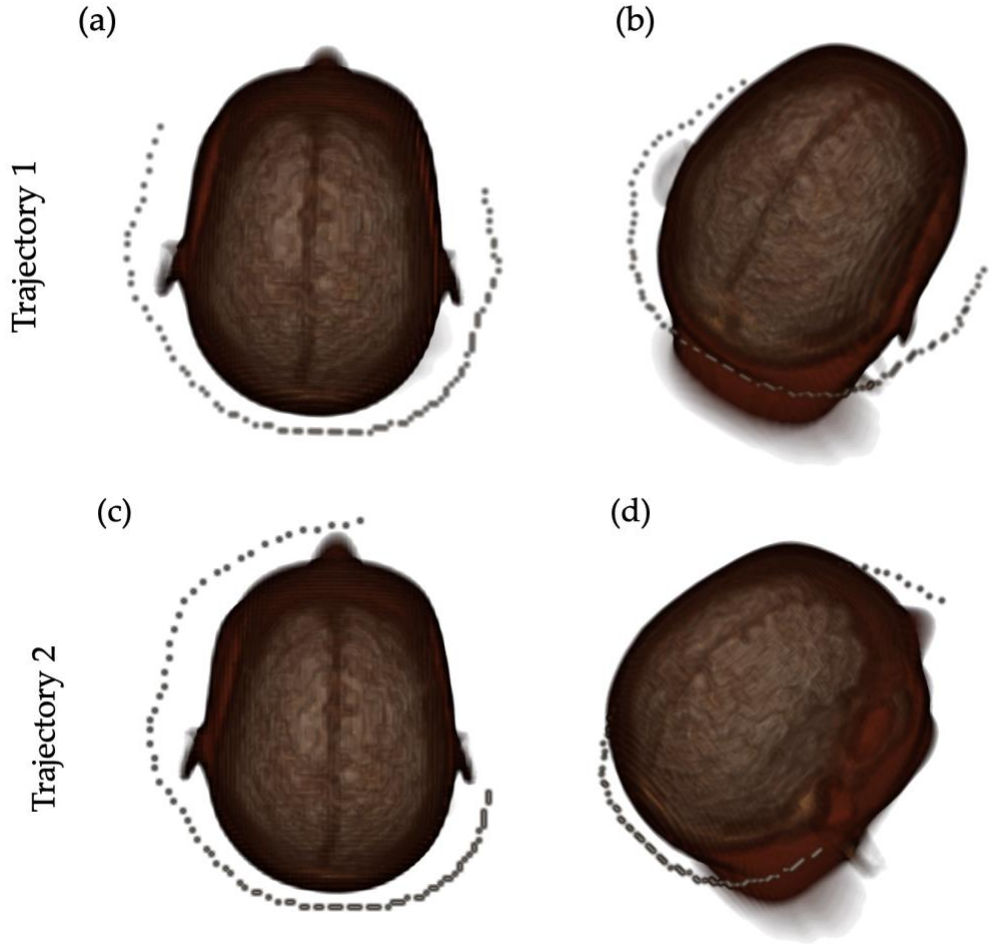

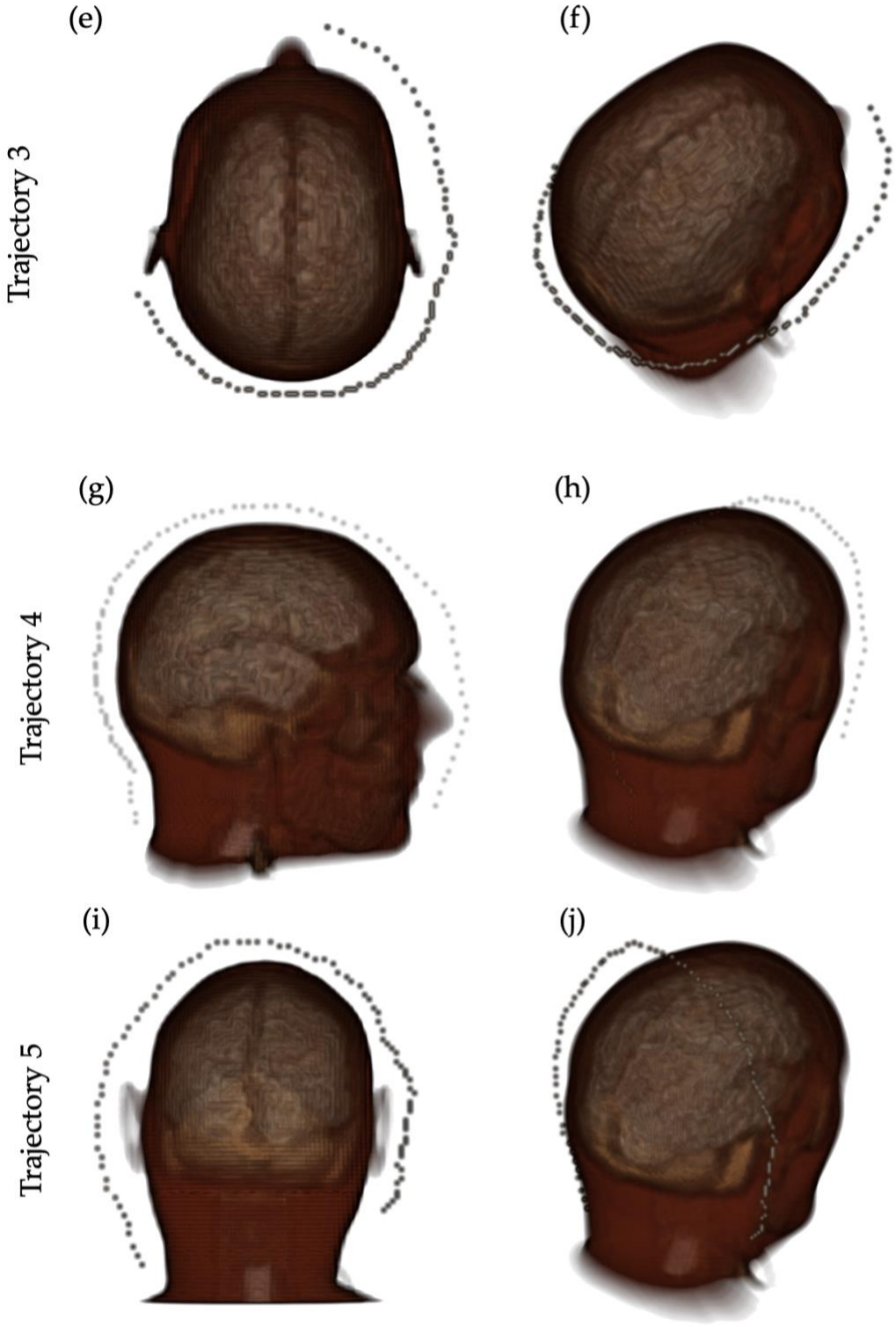
(e)
(f)
Trajectory 3
(g)
(h)
Trajectory 4
(i)
(j)
Trajectory 5

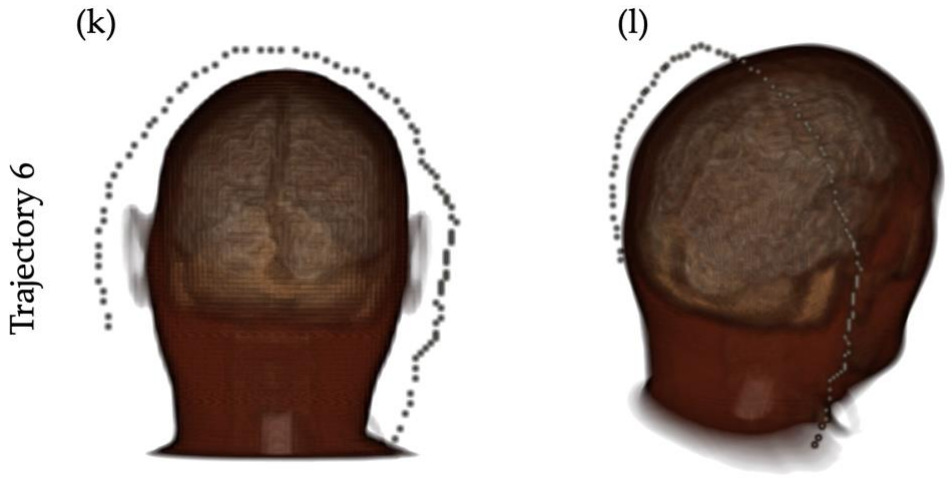

Figure 11: 3D Visualization of Pinhole Trajectories 1-6

3.2 Metrics Comparison

3.2.1 Spatial Resolution

From Fig. 13, it can be obtained that the spatial resolution in order from best to worst is trajectory 3, trajectory 1, trajectory 6, trajectory 5, trajectory 2, trajectory 4. (Smaller values indicate better spatial resolution.)

Table 2: Average Spatial Resolution of Pinhole Trajectories 1-6

Trajectory Number	Average Spatial Resolution(mm)
1	4.889
2	5.157
3	4.873
4	5.360
5	5.163
6	5.098

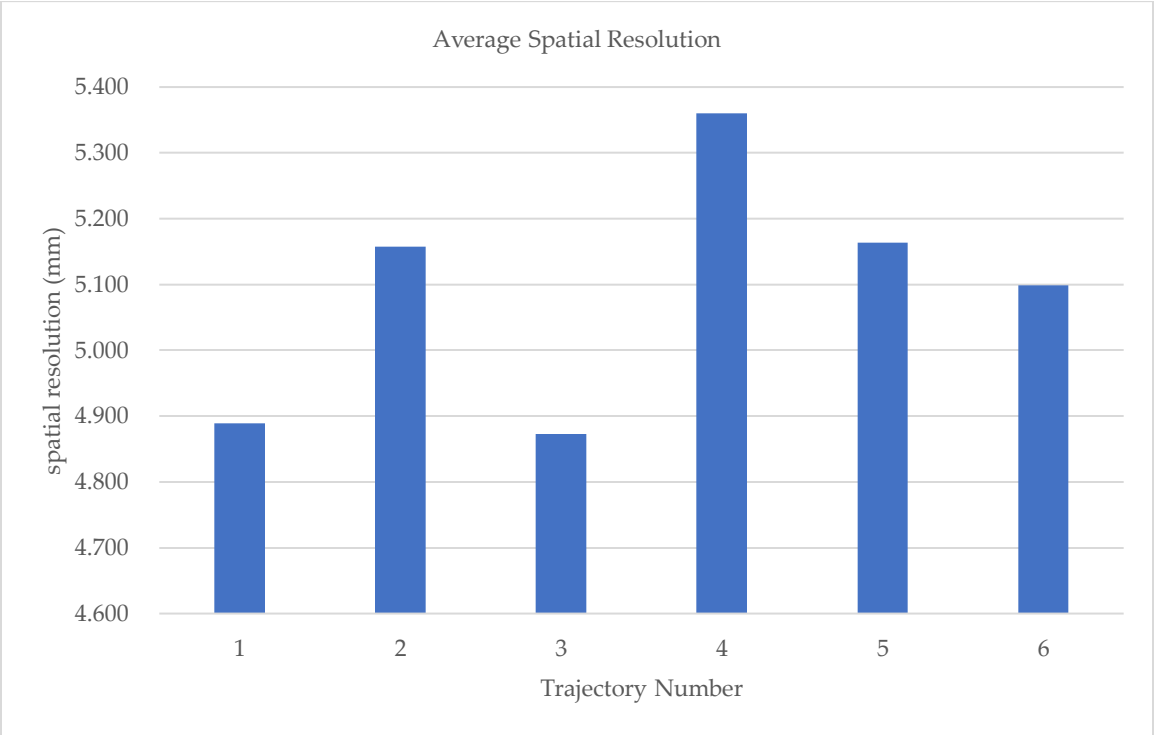

Figure 12: Average Spatial Resolution of Pinhole Trajectories 1-6

3.2.2 Geometric Efficiency

Larger values of geometric efficiency indicate better geometric efficiency. From Fig. 14, it can be obtained that the ranking of geometric efficiency from best to worst is trajectory 3, trajectory 1, trajectory 2, trajectory 6, trajectory 5, trajectory 4.

Table 3: Average Geometric Efficiency of Pinhole Trajectories 1-6

Trajectory Number	Average Geometric Efficiency
1	0.4889
2	0.5157
3	0.4873
4	0.5360
5	0.5163
6	0.5098

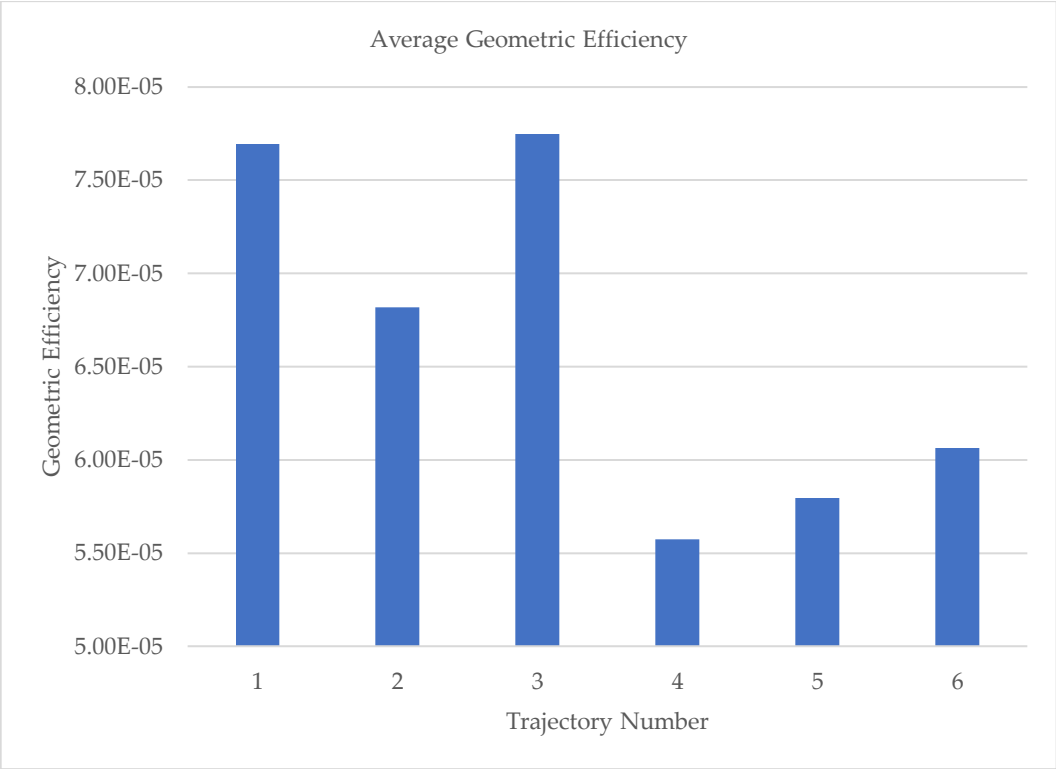

Figure 13: Average Geometric Efficiency of Pinhole Trajectories 1-6

3.2.3 Equivalent Resolution Geometric Efficiency

The equivalent-resolution geometric efficiency (ERGE) is computed using, at each pinhole location, a pinhole diameter that gives a spatial resolution of 5 mm at the COR. Larger values of ERGE indicate a better combination of efficiency and spatial resolution. From figure 14, it can be obtained that the ERGE in order from best to worst is trajectory 3, trajectory 1, trajectory 2, trajectory 6, trajectory 5, trajectory 4.

Table 4: Equivalent Resolution Geometric Efficiency of Pinhole Trajectories 1-6

Trajectory Number	ERGE
1	9.01E-05
2	7.88E-05
3	9.07E-05
4	6.02E-05
5	6.17E-05
6	6.54E-05

Figure 14: Equivalent Resolution Geometric Efficiency of Pinhole Trajectories 1-6

3.2.4 Root Mean Square Error Comparison

The SPECT images were generated using 15 subsets for OSEM reconstruction with a total of 30 iterations. Figure 15 shows the reconstructed images of trajectories 1-6. As the number of iterations increases, the contrast of the image is enhanced.

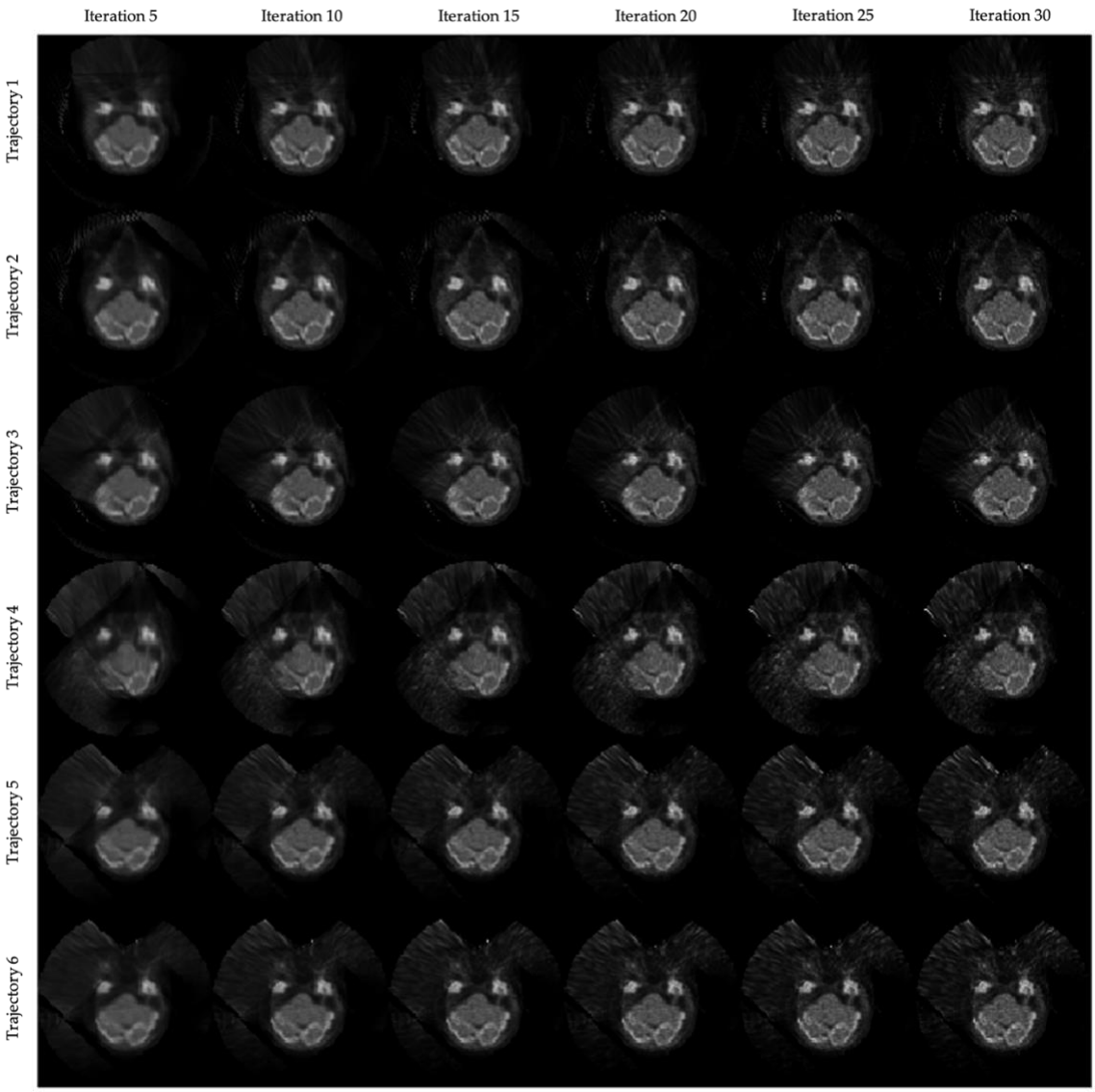

Figure 15: OSEM Images

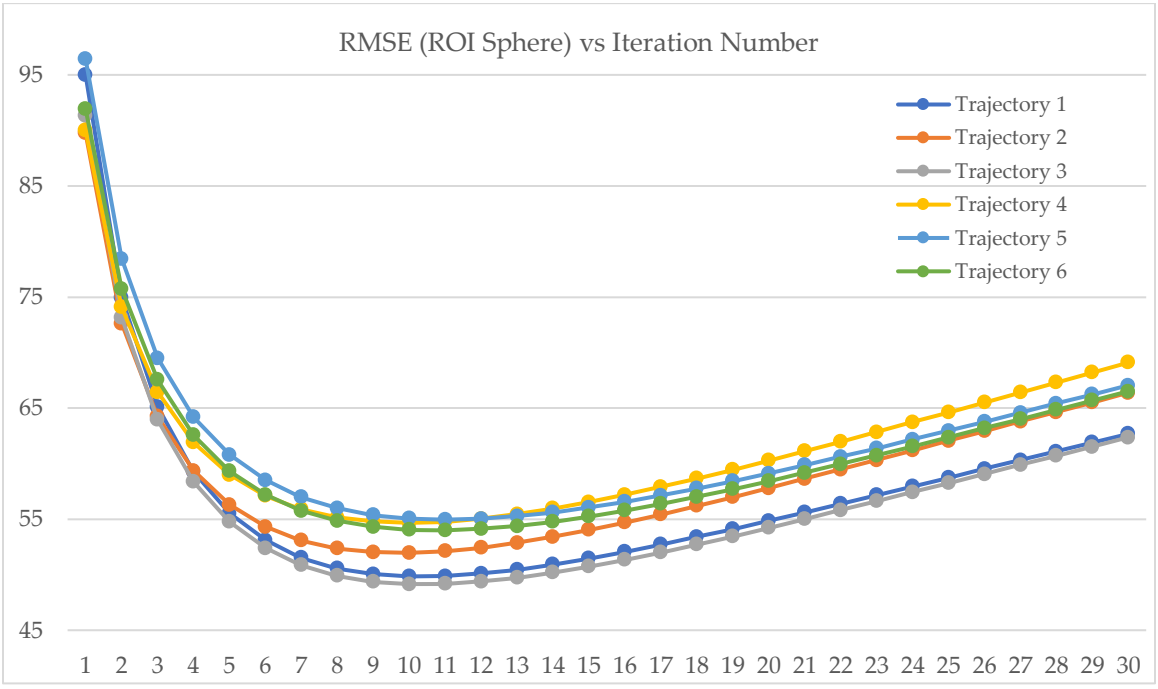

Figure 16: ROI Sphere RMSE of Pinhole Trajectories 1-6

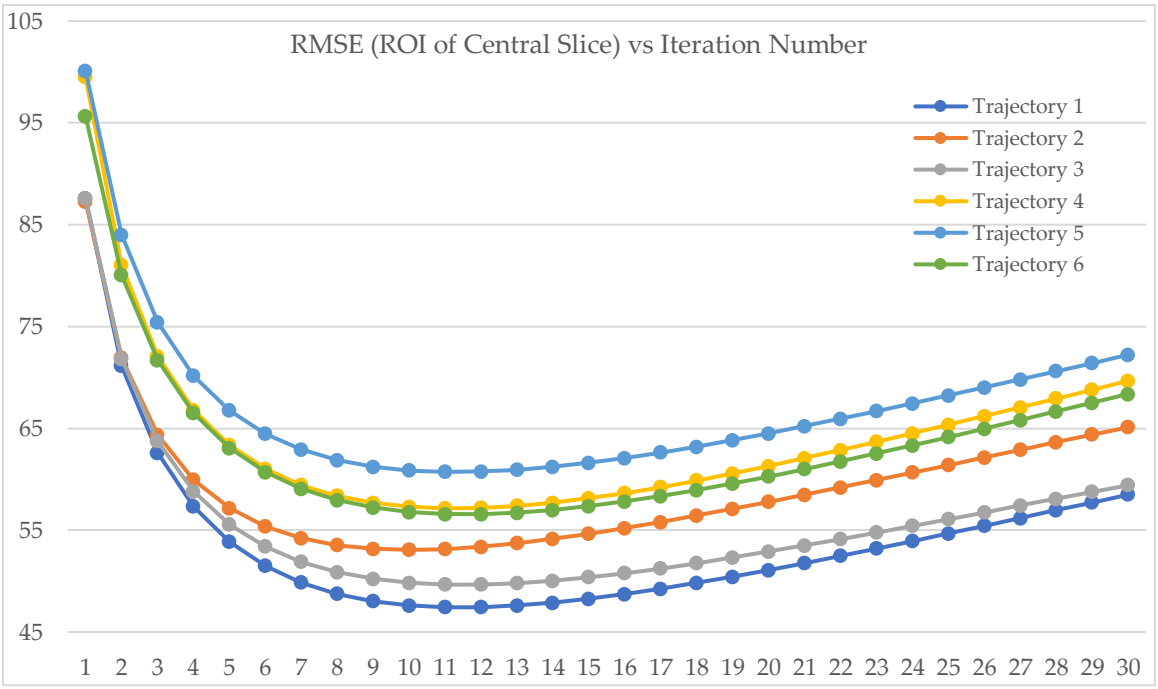

Figure 17: 40th Slice ROI RMSE of Pinhole Trajectories 1-6

Table 5: ROI RMSE of Central Slice and Entire Sphere of Pinhole Trajectories 1-6

Trajectory Number	Central Slice		Entire Sphere	
	Minimum RMSE	Iteration Number	Minimum RMSE	Iteration Number
1	47.432137	11	49.843746	10
2	53.071957	10	51.96619	10
3	49.663841	12	49.153736	10
4	57.144062	11	54.666718	10
5	60.723129	11	54.953022	11
6	56.572689	12	53.988796	11

Figure 16 shows the variation of RMSE with the number of iterations for the whole spherical ROI. Trajectory 3 always has the lowest RMSE, which indicates that it has the best reconstructed image. The ERGE of trajectory 1 is slightly lower than trajectory 3, and the RMSE performs similarly slightly worse than that of trajectory 3. Although the RMSE performance from best to worst is trajectory 3-1-2-6-4-5 in the ranking considering only the minimum RMSE, the performance from best to worst from the 11^{th} iteration is trajectory 3-1-2-6-5-4, which is exactly the same as the ranking of ERGE.

Figure 17 shows the variation of RMSE with the number of iterations for the central transverse slice of the ROI. The ranking from best to worst is trajectory 1-3-2-6-4-

5, which differs in part from the ERGE ranking. The main reason is that the trajectories are in different planes, but the ROI used for comparison is the middle slice of the transverse plane.

Trajectory 3 has the highest ERGE, and From Fig. 16 and 17, the best OSEM reconstructions (in the sense of minimum RMSE) are with trajectory 1 and trajectory 3. Trajectory 1 has a better RMSE central-slice ROI and trajectory 3 has a better RMSE entire-ROI sphere. Trajectories 4, 5, and 6 are far inferior to trajectories 1-3 in the ERGE and remain so in the OSEM reconstruction RMSE.

4. Discussion

Trajectory 3 and trajectory 1 have the highest ERGE, and From Fig. 16 and 17, the best OSEM reconstructions (in the sense of minimum RMSE) are with trajectory 1 and trajectory 3. Trajectory 1 has a better RMSE for the central-slice ROI and trajectory 3 has a better RMSE for the entire-ROI sphere. Trajectories 4-6 are far inferior to trajectories 1-3 in the ERGE and remain so in the OSEM reconstruction RMSE.

The parameters involved in the calculation of ERGE for different trajectories include spatial resolution, pinhole focal length, and ROR. The former two are the same for any trajectory, so ERGE is a function of ROR.

The process of calculating ERGE is very fast. It takes only a few minutes of user time to implement one trajectory using software such as Microsoft Excel, and the calculation is then essentially instant. In contrast, the validation process, which starts with forward projection, then adds noise, followed by OSEM reconstruction to obtain image results, is cumbersome to implement and takes more than 10 hours of computation, and the time increases with the number of set iterations.

Limitations of this study include:

(1) Not considering of attenuation and scatter. They have an impact on imaging.

(2) The only trajectories considered were trajectories contained in a 2D plane, with the COR on the centerline of the pinhole ($\theta = 0°$). In some research studies, 3D

pinhole trajectories are proposed, such as helical trajectories [16]. Trajectories in which θ is sometimes non-zero have also been considered in clinical and scientific studies [17][18].

(3) RMS error is the only metric that was considered for image quality.

Future work might consider attenuation and scatter, trajectories in different planes or 3D trajectories, and less overlap between trajectories.

5. Conclusions

In this study, a relatively simple low-cost prospective method for selecting the optimal SPECT pinhole trajectory has been shown to be effective. Only very fast and simple calculations are required. Simulation or acquisition of projection data is not needed, nor is subsequent image reconstruction. The ranking of ERGE matches well with the RMSE. In clinical and scientific research, many different pinhole trajectories might be considered for pinhole 3D SPECT imaging, but it is too time-consuming to assess each trajectory via reconstructed images. By demonstrating the validity of this method for assessing trajectories, it may facilitate the improved use of 3D pinhole SPECT imaging in clinical and scientific research.

Appendix A

Table 6: Parameters and ERGE Calculation of Trajectory 1

b/ROR(cm)	R (cm)	f(cm)	d(cm)	ERGE	b/ROR(cm)	R (cm)	f(cm)	d(cm)	ERGE
10.5	0.5	15	2.9412E-01	4.9039E-05	7.1	0.5	15	3.3937E-01	1.4279E-04
10.2	0.5	15	2.9762E-01	5.3211E-05	7.2	0.5	15	3.3784E-01	1.3760E-04
9.9	0.5	15	3.0120E-01	5.7854E-05	7.3	0.5	15	3.3632E-01	1.3266E-04
9.6	0.5	15	3.0488E-01	6.3036E-05	7.4	0.5	15	3.3482E-01	1.2795E-04
9.3	0.5	15	3.0864E-01	6.8837E-05	7.5	0.5	15	3.3333E-01	1.2346E-04
9.2	0.5	15	3.0992E-01	7.0924E-05	7.6	0.5	15	3.3186E-01	1.1917E-04
9.1	0.5	15	3.1120E-01	7.3095E-05	7.7	0.5	15	3.3040E-01	1.1507E-04
9	0.5	15	3.1250E-01	7.5352E-05	7.8	0.5	15	3.2895E-01	1.1116E-04
9	0.5	15	3.1250E-01	7.5352E-05	7.9	0.5	15	3.2751E-01	1.0742E-04
8.8	0.5	15	3.1513E-01	8.0146E-05	8	0.5	15	3.2609E-01	1.0384E-04
8.4	0.5	15	3.2051E-01	9.0994E-05	8.2	0.5	15	3.2328E-01	9.7140E-05
8.2	0.5	15	3.2328E-01	9.7140E-05	8.4	0.5	15	3.2051E-01	9.0994E-05
8	0.5	15	3.2609E-01	1.0384E-04	8.6	0.5	15	3.1780E-01	8.5346E-05
7.8	0.5	15	3.2895E-01	1.1116E-04	8.7	0.5	15	3.1646E-01	8.2693E-05
7.4	0.5	15	3.3482E-01	1.2795E-04	9.2	0.5	15	3.0992E-01	7.0924E-05
7.1	0.5	15	3.3937E-01	1.4279E-04	9.4	0.5	15	3.0738E-01	6.6829E-05
7.1	0.5	15	3.3937E-01	1.4279E-04	9.6	0.5	15	3.0488E-01	6.3036E-05
7.1	0.5	15	3.3937E-01	1.4279E-04	9.8	0.5	15	3.0242E-01	5.9518E-05
7.1	0.5	15	3.3937E-01	1.4279E-04	10	0.5	15	3.0000E-01	5.6250E-05
7.1	0.5	15	3.3937E-01	1.4279E-04	10.2	0.5	15	2.9762E-01	5.3211E-05
7.1	0.5	15	3.3937E-01	1.4279E-04	10.4	0.5	15	2.9528E-01	5.0381E-05
7.1	0.5	15	3.3937E-01	1.4279E-04	10.6	0.5	15	2.9297E-01	4.7743E-05
7.1	0.5	15	3.3937E-01	1.4279E-04	10.8	0.5	15	2.9070E-01	4.5281E-05
7.1	0.5	15	3.3937E-01	1.4279E-04	11	0.5	15	2.8846E-01	4.2980E-05
7.1	0.5	15	3.3937E-01	1.4279E-04	11.2	0.5	15	2.8626E-01	4.0829E-05
7.1	0.5	15	3.3937E-01	1.4279E-04	11.4	0.5	15	2.8409E-01	3.8814E-05
7.1	0.5	15	3.3937E-01	1.4279E-04	11.6	0.5	15	2.8195E-01	3.6925E-05
7.1	0.5	15	3.3937E-01	1.4279E-04	11.8	0.5	15	2.7985E-01	3.5154E-05
7.1	0.5	15	3.3937E-01	1.4279E-04	12	0.5	15	2.7778E-01	3.3490E-05
7.1	0.5	15	3.3937E-01	1.4279E-04	12.5	0.5	15	2.7273E-01	2.9752E-05
7.1	0.5	15	3.3937E-01	1.4279E-04	13	0.5	15	2.6786E-01	2.6534E-05
7.1	0.5	15	3.3937E-01	1.4279E-04	13.5	0.5	15	2.6316E-01	2.3749E-05
7.1	0.5	15	3.3937E-01	1.4279E-04	13.8	0.5	15	2.6042E-01	2.2257E-05
7.1	0.5	15	3.3937E-01	1.4279E-04	14.1	0.5	15	2.5773E-01	2.0882E-05
7.1	0.5	15	3.3937E-01	1.4279E-04	14.4	0.5	15	2.5510E-01	1.9615E-05
7.1	0.5	15	3.3937E-01	1.4279E-04	14.7	0.5	15	2.5253E-01	1.8444E-05
7.1	0.5	15	3.3937E-01	1.4279E-04	14.7	0.5	15	2.5253E-01	1.8444E-05
7.1	0.5	15	3.3937E-01	1.4279E-04	14.7	0.5	15	2.5253E-01	1.8444E-05
7.1	0.5	15	3.3937E-01	1.4279E-04	14.7	0.5	15	2.5253E-01	1.8444E-05
7.1	0.5	15	3.3937E-01	1.4279E-04	14.7	0.5	15	2.5253E-01	1.8444E-05
7.1	0.5	15	3.3937E-01	1.4279E-04	15.1	0.5	15	2.4917E-01	1.7018E-05
7.1	0.5	15	3.3937E-01	1.4279E-04	15.5	0.5	15	2.4590E-01	1.5730E-05
7.1	0.5	15	3.3937E-01	1.4279E-04	15.9	0.5	15	2.4272E-01	1.4564E-05
7.1	0.5	15	3.3937E-01	1.4279E-04	16.3	0.5	15	2.3962E-01	1.3506E-05
7.1	0.5	15	3.3937E-01	1.4279E-04	16.7	0.5	15	2.3659E-01	1.2544E-05
Mean ERGE					9.0097E-05				

Table 7: Parameters and ERGE Calculation of Trajectory 2

b/ROR(cm)	R (cm)	f(cm)	d(cm)	ERGE	b/ROR(cm)	R (cm)	f(cm)	d(cm)	ERGE
7.1	0.5	15	3.3937E-01	1.4279E-04	9.4	0.5	15	3.0738E-01	6.6829E-05
7.1	0.5	15	3.3937E-01	1.4279E-04	9.6	0.5	15	3.0488E-01	6.3036E-05
7.1	0.5	15	3.3937E-01	1.4279E-04	9.8	0.5	15	3.0242E-01	5.9518E-05
7.1	0.5	15	3.3937E-01	1.4279E-04	10	0.5	15	3.0000E-01	5.6250E-05
7.1	0.5	15	3.3937E-01	1.4279E-04	10.2	0.5	15	2.9762E-01	5.3211E-05
7.1	0.5	15	3.3937E-01	1.4279E-04	10.4	0.5	15	2.9528E-01	5.0381E-05
7.1	0.5	15	3.3937E-01	1.4279E-04	10.6	0.5	15	2.9297E-01	4.7743E-05
7.1	0.5	15	3.3937E-01	1.4279E-04	10.8	0.5	15	2.9070E-01	4.5281E-05
7.1	0.5	15	3.3937E-01	1.4279E-04	11	0.5	15	2.8846E-01	4.2980E-05
7.1	0.5	15	3.3937E-01	1.4279E-04	11.2	0.5	15	2.8626E-01	4.0829E-05
7.1	0.5	15	3.3937E-01	1.4279E-04	11.4	0.5	15	2.8409E-01	3.8814E-05
7.1	0.5	15	3.3937E-01	1.4279E-04	11.6	0.5	15	2.8195E-01	3.6925E-05
7.1	0.5	15	3.3937E-01	1.4279E-04	11.8	0.5	15	2.7985E-01	3.5154E-05
7.1	0.5	15	3.3937E-01	1.4279E-04	12	0.5	15	2.7778E-01	3.3490E-05
7.1	0.5	15	3.3937E-01	1.4279E-04	12.5	0.5	15	2.7273E-01	2.9752E-05
7.1	0.5	15	3.3937E-01	1.4279E-04	13	0.5	15	2.6786E-01	2.6534E-05
7.1	0.5	15	3.3937E-01	1.4279E-04	13.5	0.5	15	2.6316E-01	2.3749E-05
7.1	0.5	15	3.3937E-01	1.4279E-04	13.8	0.5	15	2.6042E-01	2.2257E-05
7.1	0.5	15	3.3937E-01	1.4279E-04	14.1	0.5	15	2.5773E-01	2.0882E-05
7.1	0.5	15	3.3937E-01	1.4279E-04	14.4	0.5	15	2.5510E-01	1.9615E-05
7.1	0.5	15	3.3937E-01	1.4279E-04	14.7	0.5	15	2.5253E-01	1.8444E-05
7.1	0.5	15	3.3937E-01	1.4279E-04	14.7	0.5	15	2.5253E-01	1.8444E-05
7.1	0.5	15	3.3937E-01	1.4279E-04	14.7	0.5	15	2.5253E-01	1.8444E-05
7.1	0.5	15	3.3937E-01	1.4279E-04	14.7	0.5	15	2.5253E-01	1.8444E-05
7.1	0.5	15	3.3937E-01	1.4279E-04	14.7	0.5	15	2.5253E-01	1.8444E-05
7.1	0.5	15	3.3937E-01	1.4279E-04	15.1	0.5	15	2.4917E-01	1.7018E-05
7.1	0.5	15	3.3937E-01	1.4279E-04	15.5	0.5	15	2.4590E-01	1.5730E-05
7.1	0.5	15	3.3937E-01	1.4279E-04	15.9	0.5	15	2.4272E-01	1.4564E-05
7.1	0.5	15	3.3937E-01	1.4279E-04	16.3	0.5	15	2.3962E-01	1.3506E-05
7.1	0.5	15	3.3937E-01	1.4279E-04	16.7	0.5	15	2.3659E-01	1.2544E-05
7.1	0.5	15	3.3937E-01	1.4279E-04	17	0.5	15	2.3438E-01	1.1880E-05
7.2	0.5	15	3.3784E-01	1.3760E-04	17	0.5	15	2.3438E-01	1.1880E-05
7.3	0.5	15	3.3632E-01	1.3266E-04	17	0.5	15	2.3438E-01	1.1880E-05
7.4	0.5	15	3.3482E-01	1.2795E-04	17	0.5	15	2.3438E-01	1.1880E-05
7.5	0.5	15	3.3333E-01	1.2346E-04	17	0.5	15	2.3438E-01	1.1880E-05
7.6	0.5	15	3.3186E-01	1.1917E-04	17	0.5	15	2.3438E-01	1.1880E-05
7.7	0.5	15	3.3040E-01	1.1507E-04	17	0.5	15	2.3438E-01	1.1880E-05
7.8	0.5	15	3.2895E-01	1.1116E-04	17	0.5	15	2.3438E-01	1.1880E-05
7.9	0.5	15	3.2751E-01	1.0742E-04	17	0.5	15	2.3438E-01	1.1880E-05
8	0.5	15	3.2609E-01	1.0384E-04	17	0.5	15	2.3438E-01	1.1880E-05
8.2	0.5	15	3.2328E-01	9.7140E-05	17	0.5	15	2.3438E-01	1.1880E-05
8.4	0.5	15	3.2051E-01	9.0994E-05	17	0.5	15	2.3438E-01	1.1880E-05
8.6	0.5	15	3.1780E-01	8.5346E-05	17	0.5	15	2.3438E-01	1.1880E-05
8.7	0.5	15	3.1646E-01	8.2693E-05	17	0.5	15	2.3438E-01	1.1880E-05
9.2	0.5	15	3.0992E-01	7.0924E-05	17	0.5	15	2.3438E-01	1.1880E-05
Mean ERGE					7.8766E-05				

Table 8: Parameters and ERGE Calculation of Trajectory 3

b/ROR(cm)	R (cm)	f(cm)	d(cm)	ERGE	b/ROR(cm)	R (cm)	f(cm)	d(cm)	ERGE
17	0.5	15	2.3438E-01	1.1880E-05	7.1	0.5	15	3.3937E-01	1.4279E-04
16.7	0.5	15	2.3659E-01	1.2544E-05	7.1	0.5	15	3.3937E-01	1.4279E-04
16.4	0.5	15	2.3885E-01	1.3257E-05	7.1	0.5	15	3.3937E-01	1.4279E-04
16.1	0.5	15	2.4116E-01	1.4023E-05	7.1	0.5	15	3.3937E-01	1.4279E-04
15.8	0.5	15	2.4351E-01	1.4845E-05	7.1	0.5	15	3.3937E-01	1.4279E-04
15.5	0.5	15	2.4590E-01	1.5730E-05	7.1	0.5	15	3.3937E-01	1.4279E-04
15	0.5	15	2.5000E-01	1.7361E-05	7.1	0.5	15	3.3937E-01	1.4279E-04
14.5	0.5	15	2.5424E-01	1.9214E-05	7.1	0.5	15	3.3937E-01	1.4279E-04
14	0.5	15	2.5862E-01	2.1328E-05	7.1	0.5	15	3.3937E-01	1.4279E-04
13.5	0.5	15	2.6316E-01	2.3749E-05	7.1	0.5	15	3.3937E-01	1.4279E-04
13	0.5	15	2.6786E-01	2.6534E-05	7.1	0.5	15	3.3937E-01	1.4279E-04
12.5	0.5	15	2.7273E-01	2.9752E-05	7.1	0.5	15	3.3937E-01	1.4279E-04
12	0.5	15	2.7778E-01	3.3490E-05	7.1	0.5	15	3.3937E-01	1.4279E-04
11.5	0.5	15	2.8302E-01	3.7854E-05	7.1	0.5	15	3.3937E-01	1.4279E-04
11	0.5	15	2.8846E-01	4.2980E-05	7.1	0.5	15	3.3937E-01	1.4279E-04
10.5	0.5	15	2.9412E-01	4.9039E-05	7.1	0.5	15	3.3937E-01	1.4279E-04
10.2	0.5	15	2.9762E-01	5.3211E-05	7.2	0.5	15	3.3784E-01	1.3760E-04
9.9	0.5	15	3.0120E-01	5.7854E-05	7.3	0.5	15	3.3632E-01	1.3266E-04
9.6	0.5	15	3.0488E-01	6.3036E-05	7.4	0.5	15	3.3482E-01	1.2795E-04
9.3	0.5	15	3.0864E-01	6.8837E-05	7.5	0.5	15	3.3333E-01	1.2346E-04
9.2	0.5	15	3.0992E-01	7.0924E-05	7.6	0.5	15	3.3186E-01	1.1917E-04
9.1	0.5	15	3.1120E-01	7.3095E-05	7.7	0.5	15	3.3040E-01	1.1507E-04
9	0.5	15	3.1250E-01	7.5352E-05	7.8	0.5	15	3.2895E-01	1.1116E-04
9	0.5	15	3.1250E-01	7.5352E-05	7.9	0.5	15	3.2751E-01	1.0742E-04
8.8	0.5	15	3.1513E-01	8.0146E-05	8	0.5	15	3.2609E-01	1.0384E-04
8.4	0.5	15	3.2051E-01	9.0994E-05	8.2	0.5	15	3.2328E-01	9.7140E-05
8.2	0.5	15	3.2328E-01	9.7140E-05	8.4	0.5	15	3.2051E-01	9.0994E-05
8	0.5	15	3.2609E-01	1.0384E-04	8.6	0.5	15	3.1780E-01	8.5346E-05
7.8	0.5	15	3.2895E-01	1.1116E-04	8.7	0.5	15	3.1646E-01	8.2693E-05
7.4	0.5	15	3.3482E-01	1.2795E-04	9.2	0.5	15	3.0992E-01	7.0924E-05
7.1	0.5	15	3.3937E-01	1.4279E-04	9.4	0.5	15	3.0738E-01	6.6829E-05
7.1	0.5	15	3.3937E-01	1.4279E-04	9.6	0.5	15	3.0488E-01	6.3036E-05
7.1	0.5	15	3.3937E-01	1.4279E-04	9.8	0.5	15	3.0242E-01	5.9518E-05
7.1	0.5	15	3.3937E-01	1.4279E-04	10	0.5	15	3.0000E-01	5.6250E-05
7.1	0.5	15	3.3937E-01	1.4279E-04	10.2	0.5	15	2.9762E-01	5.3211E-05
7.1	0.5	15	3.3937E-01	1.4279E-04	10.4	0.5	15	2.9528E-01	5.0381E-05
7.1	0.5	15	3.3937E-01	1.4279E-04	10.6	0.5	15	2.9297E-01	4.7743E-05
7.1	0.5	15	3.3937E-01	1.4279E-04	10.8	0.5	15	2.9070E-01	4.5281E-05
7.1	0.5	15	3.3937E-01	1.4279E-04	11	0.5	15	2.8846E-01	4.2980E-05
7.1	0.5	15	3.3937E-01	1.4279E-04	11.2	0.5	15	2.8626E-01	4.0829E-05
7.1	0.5	15	3.3937E-01	1.4279E-04	11.4	0.5	15	2.8409E-01	3.8814E-05
7.1	0.5	15	3.3937E-01	1.4279E-04	11.6	0.5	15	2.8195E-01	3.6925E-05
7.1	0.5	15	3.3937E-01	1.4279E-04	11.8	0.5	15	2.7985E-01	3.5154E-05
7.1	0.5	15	3.3937E-01	1.4279E-04	12	0.5	15	2.7778E-01	3.3490E-05
7.1	**0.5**	**15**	**3.3937E-01**	**1.4279E-04**	12.5	0.5	15	2.7273E-01	2.9752E-05
Mean ERGE					9.0718E-05				

Table 9: Parameters and ERGE Calculation of Trajectory 4

b/ROR(cm)	R (cm)	f(cm)	d(cm)	ERGE	b/ROR(cm)	R (cm)	f(cm)	d(cm)	ERGE
10	0.5	15	3.0000E-01	5.6250E-05	11.4	0.5	15	2.8409E-01	3.8814E-05
9.5	0.5	15	3.0612E-01	6.4897E-05	11.7	0.5	15	2.8090E-01	3.6025E-05
9	0.5	15	3.1250E-01	7.5352E-05	12	0.5	15	2.7778E-01	3.3490E-05
8.5	0.5	15	3.1915E-01	8.8111E-05	12	0.5	15	2.7778E-01	3.3490E-05
8	0.5	15	3.2609E-01	1.0384E-04	12.2	0.5	15	2.7574E-01	3.1926E-05
7.1	0.5	15	3.3937E-01	1.4279E-04	12.4	0.5	15	2.7372E-01	3.0455E-05
7.1	0.5	15	3.3937E-01	1.4279E-04	12.6	0.5	15	2.7174E-01	2.9070E-05
7.1	0.5	15	3.3937E-01	1.4279E-04	12.8	0.5	15	2.6978E-01	2.7765E-05
7.1	0.5	15	3.3937E-01	1.4279E-04	13	0.5	15	2.6786E-01	2.6534E-05
7.1	0.5	15	3.3937E-01	1.4279E-04	13.2	0.5	15	2.6596E-01	2.5372E-05
7.1	0.5	15	3.3937E-01	1.4279E-04	13.4	0.5	15	2.6408E-01	2.4275E-05
7.1	0.5	15	3.3937E-01	1.4279E-04	13.6	0.5	15	2.6224E-01	2.3238E-05
7.1	0.5	15	3.3937E-01	1.4279E-04	13.8	0.5	15	2.6042E-01	2.2257E-05
7.1	0.5	15	3.3937E-01	1.4279E-04	14	0.5	15	2.5862E-01	2.1328E-05
7.1	0.5	15	3.3937E-01	1.4279E-04	14.2	0.5	15	2.5685E-01	2.0448E-05
7.1	0.5	15	3.3937E-01	1.4279E-04	14.4	0.5	15	2.5510E-01	1.9615E-05
7.1	0.5	15	3.3937E-01	1.4279E-04	14.6	0.5	15	2.5338E-01	1.8824E-05
7.1	0.5	15	3.3937E-01	1.4279E-04	14.8	0.5	15	2.5168E-01	1.8074E-05
7.1	0.5	15	3.3937E-01	1.4279E-04	15	0.5	15	2.5000E-01	1.7361E-05
7.2	0.5	15	3.3784E-01	1.3760E-04	15.2	0.5	15	2.4834E-01	1.6684E-05
7.3	0.5	15	3.3632E-01	1.3266E-04	15.4	0.5	15	2.4671E-01	1.6040E-05
7.4	0.5	15	3.3482E-01	1.2795E-04	15.6	0.5	15	2.4510E-01	1.5428E-05
7.5	0.5	15	3.3333E-01	1.2346E-04	15.8	0.5	15	2.4351E-01	1.4845E-05
7.6	0.5	15	3.3186E-01	1.1917E-04	16	0.5	15	2.4194E-01	1.4290E-05
7.7	0.5	15	3.3040E-01	1.1507E-04	16.2	0.5	15	2.4038E-01	1.3761E-05
7.8	0.5	15	3.2895E-01	1.1116E-04	16.4	0.5	15	2.3885E-01	1.3257E-05
7.9	0.5	15	3.2751E-01	1.0742E-04	16.6	0.5	15	2.3734E-01	1.2777E-05
8	0.5	15	3.2609E-01	1.0384E-04	16.8	0.5	15	2.3585E-01	1.2318E-05
8	0.5	15	3.2609E-01	1.0384E-04	17	0.5	15	2.3438E-01	1.1880E-05
8.2	0.5	15	3.2328E-01	9.7140E-05	17	0.5	15	2.3438E-01	1.1880E-05
8.4	0.5	15	3.2051E-01	9.0994E-05	17	0.5	15	2.3438E-01	1.1880E-05
8.6	0.5	15	3.1780E-01	8.5346E-05	17	0.5	15	2.3438E-01	1.1880E-05
8.8	0.5	15	3.1513E-01	8.0146E-05	17	0.5	15	2.3438E-01	1.1880E-05
9	0.5	15	3.1250E-01	7.5352E-05	17	0.5	15	2.3438E-01	1.1880E-05
9.2	0.5	15	3.0992E-01	7.0924E-05	17	0.5	15	2.3438E-01	1.1880E-05
9.4	0.5	15	3.0738E-01	6.6829E-05	17	0.5	15	2.3438E-01	1.1880E-05
9.6	0.5	15	3.0488E-01	6.3036E-05	17.5	0.5	15	2.3077E-01	1.0868E-05
9.8	0.5	15	3.0242E-01	5.9518E-05	17.5	0.5	15	2.3077E-01	1.0868E-05
10	0.5	15	3.0000E-01	5.6250E-05	17.4	0.5	15	2.3148E-01	1.1062E-05
10.2	0.5	15	2.9762E-01	5.3211E-05	17.3	0.5	15	2.3220E-01	1.1259E-05
10.4	0.5	15	2.9528E-01	5.0381E-05	17.2	0.5	15	2.3292E-01	1.1461E-05
10.6	0.5	15	2.9297E-01	4.7743E-05	17.1	0.5	15	2.3364E-01	1.1668E-05
10.8	0.5	15	2.9070E-01	4.5281E-05	17	0.5	15	2.3438E-01	1.1880E-05
11	0.5	15	2.8846E-01	4.2980E-05	17	0.5	15	2.3438E-01	1.1880E-05
11.2	0.5	15	2.8626E-01	4.0829E-05	17	0.5	15	2.3438E-01	1.1880E-05
Mean ERGE					6.0236E-05				

Table 10: Parameters and ERGE Calculation of Trajectory 5

b/ROR(cm)	R (cm)	f(cm)	d(cm)	ERGE	b/ROR(cm)	R (cm)	f(cm)	d(cm)	ERGE
8	0.5	15	3.2609E-01	1.0384E-04	11.7	0.5	15	2.8090E-01	3.6025E-05
8	0.5	15	3.2609E-01	1.0384E-04	11.9	0.5	15	2.7881E-01	3.4309E-05
8	0.5	15	3.2609E-01	1.0384E-04	12.1	0.5	15	2.7675E-01	3.2696E-05
8	0.5	15	3.2609E-01	1.0384E-04	12.3	0.5	15	2.7473E-01	3.1179E-05
8	0.5	15	3.2609E-01	1.0384E-04	12.5	0.5	15	2.7273E-01	2.9752E-05
7.8	0.5	15	3.2895E-01	1.1116E-04	12.7	0.5	15	2.7076E-01	2.8408E-05
7.6	0.5	15	3.3186E-01	1.1917E-04	12.9	0.5	15	2.6882E-01	2.7140E-05
7.4	0.5	15	3.3482E-01	1.2795E-04	13.1	0.5	15	2.6690E-01	2.5945E-05
7.2	0.5	15	3.3784E-01	1.3760E-04	13.3	0.5	15	2.6502E-01	2.4816E-05
7.2	0.5	15	3.3784E-01	1.3760E-04	13.3	0.5	15	2.6502E-01	2.4816E-05
7.2	0.5	15	3.3784E-01	1.3760E-04	13.3	0.5	15	2.6502E-01	2.4816E-05
7.2	0.5	15	3.3784E-01	1.3760E-04	13.3	0.5	15	2.6502E-01	2.4816E-05
7.2	0.5	15	3.3784E-01	1.3760E-04	13.3	0.5	15	2.6502E-01	2.4816E-05
7.2	0.5	15	3.3784E-01	1.3760E-04	13.2	0.5	15	2.6596E-01	2.5372E-05
7.2	0.5	15	3.3784E-01	1.3760E-04	13.1	0.5	15	2.6690E-01	2.5945E-05
7.2	0.5	15	3.3784E-01	1.3760E-04	13	0.5	15	2.6786E-01	2.6534E-05
7.2	0.5	15	3.3784E-01	1.3760E-04	13	0.5	15	2.6786E-01	2.6534E-05
7.4	0.5	15	3.3482E-01	1.2795E-04	13	0.5	15	2.6786E-01	2.6534E-05
7.6	0.5	15	3.3186E-01	1.1917E-04	13	0.5	15	2.6786E-01	2.6534E-05
7.8	0.5	15	3.2895E-01	1.1116E-04	13	0.5	15	2.6786E-01	2.6534E-05
8	0.5	15	3.2609E-01	1.0384E-04	13.1	0.5	15	2.6690E-01	2.5945E-05
8	0.5	15	3.2609E-01	1.0384E-04	13.3	0.5	15	2.6502E-01	2.4816E-05
8	0.5	15	3.2609E-01	1.0384E-04	13.5	0.5	15	2.6316E-01	2.3749E-05
8	0.5	15	3.2609E-01	1.0384E-04	13.5	0.5	15	2.6316E-01	2.3749E-05
8	0.5	15	3.2609E-01	1.0384E-04	13.5	0.5	15	2.6316E-01	2.3749E-05
8	0.5	15	3.2609E-01	1.0384E-04	13.5	0.5	15	2.6316E-01	2.3749E-05
8	0.5	15	3.2609E-01	1.0384E-04	13.5	0.5	15	2.6316E-01	2.3749E-05
8	0.5	15	3.2609E-01	1.0384E-04	13.5	0.5	15	2.6316E-01	2.3749E-05
8	0.5	15	3.2609E-01	1.0384E-04	13.5	0.5	15	2.6316E-01	2.3749E-05
8	0.5	15	3.2609E-01	1.0384E-04	13.5	0.5	15	2.6316E-01	2.3749E-05
8.2	0.5	15	3.2328E-01	9.7140E-05	13.5	0.5	15	2.6316E-01	2.3749E-05
8.5	0.5	15	3.1915E-01	8.8111E-05	13.5	0.5	15	2.6316E-01	2.3749E-05
8.8	0.5	15	3.1513E-01	8.0146E-05	13.5	0.5	15	2.6316E-01	2.3749E-05
9.1	0.5	15	3.1120E-01	7.3095E-05	13.5	0.5	15	2.6316E-01	2.3749E-05
9.4	0.5	15	3.0738E-01	6.6829E-05	13.5	0.5	15	2.6316E-01	2.3749E-05
9.7	0.5	15	3.0364E-01	6.1244E-05	13.5	0.5	15	2.6316E-01	2.3749E-05
9.9	0.5	15	3.0120E-01	5.7854E-05	13.5	0.5	15	2.6316E-01	2.3749E-05
10.1	0.5	15	2.9880E-01	5.4703E-05	13.5	0.5	15	2.6316E-01	2.3749E-05
10.3	0.5	15	2.9644E-01	5.1771E-05	13.5	0.5	15	2.6316E-01	2.3749E-05
10.5	0.5	15	2.9412E-01	4.9039E-05	13.5	0.5	15	2.6316E-01	2.3749E-05
10.7	0.5	15	2.9183E-01	4.6491E-05	13.5	0.5	15	2.6316E-01	2.3749E-05
10.9	0.5	15	2.8958E-01	4.4111E-05	13.5	0.5	15	2.6316E-01	2.3749E-05
11.1	0.5	15	2.8736E-01	4.1887E-05	13.5	0.5	15	2.6316E-01	2.3749E-05
11.3	0.5	15	2.8517E-01	3.9805E-05	13.5	0.5	15	2.6316E-01	2.3749E-05
11.5	0.5	15	2.8302E-01	3.7854E-05	13.5	0.5	15	2.6316E-01	2.3749E-05
Mean ERGE					6.1702E-05				

Table 11: Parameters and ERGE Calculation of Trajectory 6

b/ROR(cm)	R (cm)	f(cm)	d(cm)	ERGE	b/ROR(cm)	R (cm)	f(cm)	d(cm)	ERGE
11.5	0.5	15	2.8302E-01	3.7854E-05	10.1	0.5	15	2.9880E-01	5.4703E-05
11	0.5	15	2.8846E-01	4.2980E-05	10.3	0.5	15	2.9644E-01	5.1771E-05
10.5	0.5	15	2.9412E-01	4.9039E-05	10.5	0.5	15	2.9412E-01	4.9039E-05
10	0.5	15	3.0000E-01	5.6250E-05	10.7	0.5	15	2.9183E-01	4.6491E-05
9.5	0.5	15	3.0612E-01	6.4897E-05	10.9	0.5	15	2.8958E-01	4.4111E-05
9	0.5	15	3.1250E-01	7.5352E-05	11.1	0.5	15	2.8736E-01	4.1887E-05
8.5	0.5	15	3.1915E-01	8.8111E-05	11.3	0.5	15	2.8517E-01	3.9805E-05
8	0.5	15	3.2609E-01	1.0384E-04	11.5	0.5	15	2.8302E-01	3.7854E-05
8	0.5	15	3.2609E-01	1.0384E-04	11.7	0.5	15	2.8090E-01	3.6025E-05
8	0.5	15	3.2609E-01	1.0384E-04	11.9	0.5	15	2.7881E-01	3.4309E-05
8	0.5	15	3.2609E-01	1.0384E-04	12.1	0.5	15	2.7675E-01	3.2696E-05
8	0.5	15	3.2609E-01	1.0384E-04	12.3	0.5	15	2.7473E-01	3.1179E-05
8	0.5	15	3.2609E-01	1.0384E-04	12.5	0.5	15	2.7273E-01	2.9752E-05
7.8	0.5	15	3.2895E-01	1.1116E-04	12.7	0.5	15	2.7076E-01	2.8408E-05
7.6	0.5	15	3.3186E-01	1.1917E-04	12.9	0.5	15	2.6882E-01	2.7140E-05
7.4	0.5	15	3.3482E-01	1.2795E-04	13.1	0.5	15	2.6690E-01	2.5945E-05
7.2	0.5	15	3.3784E-01	1.3760E-04	13.3	0.5	15	2.6502E-01	2.4816E-05
7.2	0.5	15	3.3784E-01	1.3760E-04	13.3	0.5	15	2.6502E-01	2.4816E-05
7.2	0.5	15	3.3784E-01	1.3760E-04	13.3	0.5	15	2.6502E-01	2.4816E-05
7.2	0.5	15	3.3784E-01	1.3760E-04	13.3	0.5	15	2.6502E-01	2.4816E-05
7.2	0.5	15	3.3784E-01	1.3760E-04	13.3	0.5	15	2.6502E-01	2.4816E-05
7.2	0.5	15	3.3784E-01	1.3760E-04	13.2	0.5	15	2.6596E-01	2.5372E-05
7.2	0.5	15	3.3784E-01	1.3760E-04	13.1	0.5	15	2.6690E-01	2.5945E-05
7.2	0.5	15	3.3784E-01	1.3760E-04	13	0.5	15	2.6786E-01	2.6534E-05
7.2	0.5	15	3.3784E-01	1.3760E-04	13	0.5	15	2.6786E-01	2.6534E-05
7.4	0.5	15	3.3482E-01	1.2795E-04	13	0.5	15	2.6786E-01	2.6534E-05
7.6	0.5	15	3.3186E-01	1.1917E-04	13	0.5	15	2.6786E-01	2.6534E-05
7.8	0.5	15	3.2895E-01	1.1116E-04	13	0.5	15	2.6786E-01	2.6534E-05
8	0.5	15	3.2609E-01	1.0384E-04	13.1	0.5	15	2.6690E-01	2.5945E-05
8	0.5	15	3.2609E-01	1.0384E-04	13.3	0.5	15	2.6502E-01	2.4816E-05
8	0.5	15	3.2609E-01	1.0384E-04	13.5	0.5	15	2.6316E-01	2.3749E-05
8	0.5	15	3.2609E-01	1.0384E-04	13.5	0.5	15	2.6316E-01	2.3749E-05
8	0.5	15	3.2609E-01	1.0384E-04	13.5	0.5	15	2.6316E-01	2.3749E-05
8	0.5	15	3.2609E-01	1.0384E-04	13.5	0.5	15	2.6316E-01	2.3749E-05
8	0.5	15	3.2609E-01	1.0384E-04	13.5	0.5	15	2.6316E-01	2.3749E-05
8	0.5	15	3.2609E-01	1.0384E-04	13.5	0.5	15	2.6316E-01	2.3749E-05
8	0.5	15	3.2609E-01	1.0384E-04	13.5	0.5	15	2.6316E-01	2.3749E-05
8	0.5	15	3.2609E-01	1.0384E-04	13.5	0.5	15	2.6316E-01	2.3749E-05
8.2	0.5	15	3.2328E-01	9.7140E-05	13.5	0.5	15	2.6316E-01	2.3749E-05
8.5	0.5	15	3.1915E-01	8.8111E-05	13.5	0.5	15	2.6316E-01	2.3749E-05
8.8	0.5	15	3.1513E-01	8.0146E-05	13.5	0.5	15	2.6316E-01	2.3749E-05
9.1	0.5	15	3.1120E-01	7.3095E-05	13.5	0.5	15	2.6316E-01	2.3749E-05
9.4	0.5	15	3.0738E-01	6.6829E-05	13.5	0.5	15	2.6316E-01	2.3749E-05
9.7	0.5	15	3.0364E-01	6.1244E-05	13.5	0.5	15	2.6316E-01	2.3749E-05
9.9	0.5	15	3.0120E-01	5.7854E-05	13.5	0.5	15	2.6316E-01	2.3749E-05
Mean ERGE					6.5350E-05				

Appendix B

Table 12: RMSE of ROI Central Slice V.S. Iteration Numbers of Trajectories 1-6

Iteration numbers	Trajectory 1	Trajectory 2	Trajectory 3	Trajectory 4	Trajectory 5	Trajectory 6
1	87.609657	87.28466	87.601738	99.500954	100.127159	95.666107
2	71.154259	71.944229	71.820946	81.046455	84.003548	80.053085
3	62.607189	64.367271	63.748463	72.10675	75.446465	71.71769
4	57.322254	59.938175	58.795929	66.805283	70.180779	66.502655
5	53.859303	57.152397	55.569702	63.363693	66.761078	63.046425
6	51.498253	55.355572	53.392555	61.033764	64.47097	60.686977
7	49.865158	54.212749	51.900059	59.438911	62.921467	59.058784
8	48.752048	53.528008	50.8866	58.365063	61.888466	57.94733
9	48.030296	53.176037	50.227379	57.679302	61.233818	57.219067
10	47.611881	53.071957	49.84016	57.293125	60.866516	56.785629
11	47.432137	53.155994	49.666775	57.144062	60.723129	56.585258
12	47.441704	53.384796	49.663841	57.185844	60.757484	56.572689
13	47.602314	53.726185	49.797897	57.382854	60.934944	56.71347
14	47.88406	54.155865	50.042557	57.706875	61.228935	56.980686
15	48.263458	54.655201	50.37674	58.135201	61.618538	57.352894
16	48.721951	55.209732	50.78344	58.649391	62.086853	57.812668
17	49.244747	55.80814	51.248852	59.234379	62.620152	58.345642
18	49.819977	56.441494	51.761734	59.877792	63.207291	58.939854
19	50.437996	57.102703	52.312881	60.569397	63.839127	59.585297
20	51.090893	57.786098	52.894733	61.300697	64.50808	60.273575
21	51.772083	58.487083	53.501049	62.064583	65.207809	60.997612
22	52.476059	59.201916	54.126667	62.855106	65.933014	61.751392
23	53.198215	59.927486	54.7673	63.667271	66.679192	62.5298
24	53.934673	60.661224	55.41938	64.49688	67.442566	63.328461
25	54.682156	61.400974	56.079945	65.340393	68.21991	64.143623
26	55.437897	62.144932	56.746513	66.194809	69.008446	64.972076
27	56.199532	62.891571	57.417034	67.05761	69.805817	65.811043
28	56.965065	63.639626	58.089787	67.926636	70.609985	66.658165
29	57.732788	64.388008	58.763336	68.800087	71.41922	67.511398
30	58.501255	65.135826	59.436489	69.676399	72.232048	68.36898
Mini	**47.432137**	**53.071957**	**49.663841**	**57.144062**	**60.723129**	**56.572689**

Table 13: RMSE of Entire Sphere V.S. Iteration Numbers of Trajectories 1-6

Iteration numbers	Trajectory 1	Trajectory 2	Trajectory 3	Trajectory 4	Trajectory 5	Trajectory 6
1	95.011444	89.751831	91.320564	90.001015	96.444351	91.936859
2	74.968697	72.6091	73.170593	74.099838	78.450455	75.735161
3	65.10743	64.239258	63.955357	66.444298	69.507423	67.534653
4	59.250561	59.352123	58.371178	61.905136	64.190979	62.560024
5	55.522877	56.286194	54.768661	59.004986	60.776917	59.334202
6	53.095066	54.32272	52.400288	57.110428	58.504616	57.187763
7	51.531231	53.090179	50.860458	55.891426	56.98204	55.761478
8	50.571381	52.371674	49.903759	55.154099	55.984283	54.842911
9	50.047184	52.028557	49.370995	54.774197	55.371086	54.297123
10	49.843746	51.96619	49.153736	54.666718	55.049103	54.033566
11	49.879818	52.117035	49.175362	54.770638	54.953022	53.988796
12	50.096584	52.431477	49.380188	55.040627	55.035336	54.116627
13	50.450787	52.872398	49.726845	55.442184	55.260406	54.382355
14	50.910206	53.411678	50.184036	55.94862	55.600872	54.759262
15	51.450626	54.027821	50.727772	56.539005	56.035263	55.226406
16	52.053658	54.704243	51.339432	57.196793	56.546471	55.767101
17	52.705215	55.428032	52.004429	57.908772	57.120647	56.367908
18	53.394398	56.189037	52.71122	58.664303	57.746513	57.017899
19	54.112671	56.979176	53.450592	59.454765	58.414764	57.708115
20	54.853275	57.791962	54.215145	60.273129	59.117714	58.431187
21	55.610821	58.622158	54.998894	61.113621	59.848953	59.180996
22	56.380943	59.465523	55.796967	61.971485	60.60313	59.952423
23	57.16011	60.318588	56.6054	62.842785	61.375767	60.741177
24	57.945419	61.178513	57.420925	63.724247	62.163094	61.543625
25	58.734493	62.042957	58.240875	64.613144	62.961941	62.356705
26	59.525364	62.909977	59.063034	65.507202	63.769627	63.177818
27	60.316406	63.777962	59.885586	66.404495	64.583885	64.004768
28	61.106266	64.645569	60.707031	67.303429	65.402794	64.835678
29	61.893826	65.511681	61.526131	68.202644	66.224716	65.668976
30	62.678162	66.375351	62.341854	69.101006	67.048264	66.503296
Mini	**49.843746**	**51.96619**	**49.153736**	**54.666718**	**54.953022**	**53.988796**

References

[1] Prince, Simon JD. *Computer vision: models, learning, and inference*. Cambridge University Press, 2012.

[2] Wanet, Patrick M., Alain Sand, and Jean Abramovici. "Physical and clinical evaluation of high-resolution thyroid pinhole tomography." *Journal of Nuclear Medicine* 37.12 (1996): 2017-2020.

[3] Tomas, Maria B., et al. "Pinhole versus parallel-hole collimators for parathyroid imaging: an intraindividual comparison." *Journal of nuclear medicine technology* 36.4 (2008): 189-194.

[4] Bowsher, James, et al. "Onboard functional and molecular imaging: A design investigation for robotic multipinhole SPECT." *Medical physics* 41.1 (2014): 010701.

[5] An, Byungho, et al. "Usefulness of 24-hour delayed bone scintigraphy of knee joint using pinhole collimator." (2014): 2625-2625.

[6] Habraken, Jan BA, et al. "Evaluation of high-resolution pinhole SPECT using a small rotating animal." *Journal of Nuclear Medicine* 42.12 (2001): 1863-1869.

[7] Chen, Ling, Benjamin MW Tsui, and Greta SP Mok. "Design and evaluation of two multi-pinhole collimators for brain SPECT." *Annals of nuclear medicine* 31.8 (2017): 636-648.

[8] Chen, Yuan, et al. "Optimized image acquisition for dopamine transporter imaging with ultra-high resolution clinical pinhole SPECT." *Physics in Medicine & Biology* 63.22 (2018): 225002.

[9] Segars, W. Paul, and Benjamin MW Tsui. "MCAT to XCAT: The evolution of 4-D computerized phantoms for imaging research." *Proceedings of the IEEE* 97.12 (2009): 1954-1968.

[10] Bowsher, James E., et al. "Regional SPECT imaging using sampling principles and multiple pinholes." *IEEE Nuclear Science Symposuim & Medical Imaging Conference*. IEEE, 2010.

[11] Bowsher, James E., et al. "Aligning emission tomography and MRI images by optimizing the emission-tomography image reconstruction objective function." *IEEE transactions on nuclear science* 53.3 (2006): 1248-1258.

[12] Metzler, Scott D., et al. "Analytic determination of pinhole collimator sensitivity with penetration." *IEEE transactions on medical imaging* 20.8 (2001): 730-741.

[13] Cherry, Simon R., et al. *Physics in Nuclear Medicine*. Elsevier/Saunders, 2012: Figure 14-20.

[14] Cherry, Simon R., et al. *Physics in Nuclear Medicine*. Elsevier/Saunders, 2012: Equations 14-16.

[15] Cherry, Simon R., et al. *Physics in Nuclear Medicine*. Elsevier/Saunders, 2012: Equations 14-15.

[16] Metzler, Scott D., et al. "Feasibility of whole-body functional mouse imaging using helical pinhole SPECT." *Molecular imaging and biology* 12.1 (2010): 35-41.

[17] Beque, Dirk, et al. "Characterization of pinhole SPECT acquisition geometry." *IEEE transactions on medical imaging* 22.5 (2003): 599-612.

[18] Cao, Zixiong, et al. "Optimal number of pinholes in multi-pinhole SPECT for mouse brain imaging—a simulation study." *Physics in Medicine & Biology* 50.19 (2005): 4609.